



Available online at www.sciencedirect.com

ScienceDirect

Advances in Space Research 68 (2021) 4434–4455

**ADVANCES IN
SPACE
RESEARCH**
(a COSPAR publication)
www.elsevier.com/locate/asr

Development of CubeSat systems in formation flying for the solar science demonstration: The CANYVAL-C mission

Geuk-Nam Kim, Sang-Young Park*, Taeyang Lee, Dae-Eun Kang, Soobin Jeon, Jihae Son
Namgyu Kim, Yeon-Kyu Park, Youngbum Song

Astrodynamics and Control Laboratory, Department of Astronomy, Yonsei University, Seoul, Republic of Korea

Received 27 January 2021; received in revised form 23 August 2021; accepted 24 September 2021

Available online 9 October 2021

Abstract

This paper presents the systems of the CANYVAL-C mission—a mission that demonstrates the concept of a virtual space telescope for a solar science mission, which is achieved by using two CubeSats (1U: Timon, 2U: Pumbaa). The aim of the mission is to capture images of the solar corona by performing precise formation flying. Two CubeSat systems were developed for this investigation: a 1U CubeSat and a 2U CubeSat. The 1U CubeSat can take several pictures of the solar corona, whereas the 2U CubeSat blocks the sunlight with its payload, which is called the Occulter. To accomplish the goal of this mission, precise guidance, navigation, and control technologies have been developed and verified through numerical simulations and the hardware-in-the loop simulations. Flight models of the two CubeSats were developed with end-to-end testing and environmental testing to ensure the feasibility of the mission operations under practical limitations. The two CubeSats are scheduled to launch and be in operation in the first half of 2021.

© 2021 COSPAR. Published by Elsevier B.V. This is an open access article under the CC BY-NC-ND license (<http://creativecommons.org/licenses/by-nc-nd/4.0/>).

Keywords: Satellite formation flying; Cube satellite; Coronagraph; System design

1. Introduction

As a part of the NewSpace concept, CubeSat has recently been enhancing opportunities for access to space (Denis et al., 2020). Because of its relatively low cost and commercial-off-the-shelf (COTS)-based fast development, the CubeSat platform is used for challenging missions as a science and technical demonstration. With these advantages, several space agencies, institutes, and universities have developed CubeSat systems with the objective of validating high-risk systems for practical reasons. The Aero-

Cube program of NASA is focused on technology development of small size, low weight, and low power platforms. This program includes missions for optical communication, miniaturized actuators, proximity operations, and the validation of flight software (Welle and Hinkley, 2020). The CubeSat Proximity Operations Demonstration (CPOD) mission by Tyvak Inc. aims to demonstrate rendezvous, proximity, and docking by using two 3U CubeSats with miniaturized avionics (Roscoe, Westphal, and Mosleh, 2018). The Canadian Advanced Nanospace eXperiment-4&5 (CanX-4&5) by UTIAS/SFL demonstrated autonomous formation flying that accomplished relative positioning maneuvers with sub-meter-level accuracy (Newman, 2015). The University of Colorado developed a 3U CubeSat, denoted the “Miniature X-ray Solar Spectrometer (MinXSS),” to study the energy distribution of solar flares (Mason et al., 2020). In addition, the CubeSat platform is applicable in areas such as interplanetary

* Corresponding author.

E-mail addresses: south1003@yonsei.ac.kr (G.-N. Kim), spar-k624@yonsei.ac.kr (S.-Y. Park), dlxodid300@gmail.com (T. Lee), rkddeodms@gmail.com (D.-E. Kang), forestine@yonsei.ac.kr (S. Jeon), son920928@gmail.com (J. Son), shephful@gmail.com (N. Kim), yeonq-park@snu.ac.kr (Y.-K. Park), v1225v@naver.com (Y. Song).

exploration (Millan et al., 2019), space structure construction (Underwood et al., 2015), and constellations for Earth observation and communication (Bandyopadhyay et al., 2015). However, when designing a mission with the CubeSat platform, constraints associated with limited resources, such as sizing, power, and communication, need to be considered.

The virtual telescope (VT) is gaining interest as a solution to address the limitations and improve the observational performance of traditional space telescopes. The VT consists of two independent spacecraft that function as a detector system and an optics system (Shah et al., 2013; Park et al., 2014; Dennis et al., 2013). This separated structure with the detector and optics systems enables the extension of the focal length. This is a promising method that is dedicated to spaceborne investigations in solar physics (Vives et al., 2009), astrophysics (Skinner et al., 2008), and exoplanet identification (Seager et al., 2015). To obtain high-quality celestial images, the optics and detector systems shall be remotely aligned with respect to the inertial target; this is defined as an inertial alignment technology (Calhoun et al., 2018). The core technology of VT aims to enable precise formation flying to provide a feasible role as a space telescope.

The CubeSat Astronomy by NASA and Yonsei using the Virtual Telescope ALignment (CANYVAL) project will implement technologies for the VT in space with CubeSat platforms. The first mission was the CANYVAL-X (eXperiment) mission, which was developed to conduct experiments and demonstrate core technologies for the inertial alignment (Park et al., 2016). The CANYVAL-C (Coronagraph) mission is the secondary phase of the CANYVAL project and it has been in development since 2017. Fig. 1 shows the concept of the CANYVAL-C mission. The goal is to demonstrate the solar field by obtaining pictures of the solar corona, including the region that is 10 times the solar angular diameter (Kim et al., 2019). The mission will prove the feasibility of real-scale solar science missions with the concept of the VT. To accomplish its objective, two CubeSat systems, 1U CubeSat and 2U CubeSat, were developed. These two systems can implement precise autonomous formation flying. Specifically, the 1U CubeSat, which is known as Timon, is equipped

with a camera for visible light. Further, the 2U CubeSat, which is known as Pumbaa, is equipped with an Occulter to block the light from the solar photosphere. It is possible to concentrate the light intensity of the solar corona by separately constructing a coronagraph structure, enabling studies for the low corona region, near the photosphere (Landini et al., 2011). The launch of the CubeSats is scheduled to take place in the first half of 2021.

The contributions of this paper are described as follows. First, the design scheme of the new solar science demonstration mission concept with formation flying CubeSat systems is presented. The key technologies for the VT were developed and validated through previous research studies (Shah et al., 2013; Park et al., 2014; Dennis et al., 2013). However, they are limited because they have only been used in laboratory settings with formation flying algorithms design and numerical studies. The significance of this study is that the feasibility of the VT technologies will be demonstrated by real-world applications with in-orbit testing. Furthermore, several full-scale missions and their systems for formation flying and solar science require relatively strict requirements that are difficult to satisfy. Herein, the systems architecture is presented. This architecture enables lower development costs and leads to a shorter development schedule before the implementation of the real-world and full-scale missions.

Secondly, the development process of the CubeSat systems with limitations on bus configurations and systems operation is also outlined, including solutions such as the systems architectures, the miniaturized components design, and operational strategies. Developing these CubeSat systems was challenging because of the restricted structural configurations from small-sized platforms with standardized COTS components. These structural limitations cause constraints on the implementation of the guidance, navigation, and control (GNC) algorithm. The limitations for this mission had been overcome with design of novel systems architecture and feasible operational strategies with ground validations. By sharing the bus and the flight software (FSW) architecture between each CubeSat, it was enabled to develop the systems simultaneously, without any loss in robustness. The electrical harnessing was simplified with two-wire and parallel interfaces. Furthermore, several components were miniaturized to save the internal space; specifically, the on-board computer (OBC) integrated with the GNSS receiver and the ultra-high frequency (UHF) transceiver, the air-coil type magnetic torquer (MTQ), the 3D printed propulsion system (PPS), and the Occulter with tape measures. The open source FSW framework that was developed by NASA is known as the core flight system (cFS) and it is applied to manipulate the complicated tasks and scheduling in the OBC (NASA/GSFC, 2020). The GNC algorithms for precise formation flying were developed. Then, the global navigation service system (GNSS), the inter-satellite link (ISL), the three-axis reaction wheel assembly (RWA), and the PPS with a cold gas thruster were used for the implementation of the GNC. The differ-

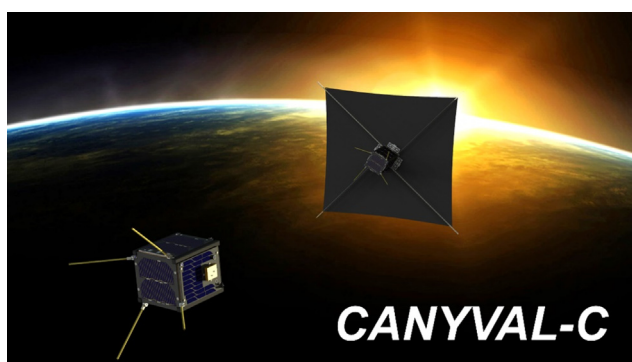


Fig. 1. Concept of the CANYVAL-C mission.

ential atmospheric drag control (DADC) technique was applied to maintain the relative distance between the CubeSats, which is a propellantless orbit maneuver method. In addition, to deal with a low visibility of GNSS signals during a relative navigation, the orientations of each CubeSat were defined.

Finally, the verifications and validations conducted to ensure the completion of the challenging mission using CubeSat platforms, including the hardware-in-the-loop simulation (HILS) for the GNC algorithms and testing for the integrated CubeSat systems, are discussed. The GNC algorithm was verified through the HILS as well as numerical simulations. For validation of the constructed systems, end-to-end testing and environment testing were conducted.

The remainder of this paper is organized as follows. **Section 2** describes in detail the CANYVAL-C mission, including the allocation of mission requirements and the operating concept. **Section 3** covers the systems design of the two CubeSats for autonomous and precise formation flying missions. **Section 4** discusses the systems analyses conducted for mission assurance, which includes performance analysis of the attitude, orbit determination, control algorithms, and the power management. **Section 5** describes the CubeSat systems assembly, integration, and verification processes as well as the specifications of each CubeSat. Finally, **Section 6** summarizes the study and presents concluding remarks.

2. CANYVAL-mission description

The CANYVAL-C mission applies the concept of the VT by using two CubeSats. The aim of the mission is to take images of the solar corona via formation flying. During the mission operations, Timon (1U CubeSat) and Pumbaa (2U CubeSat) are aligned with respect to the sun remotely while holding the relative distance, which is defined as the inertial alignment and hold (IAH). The light of the solar photosphere is hidden by the Occulter. Subsequently, Timon obtains the images of the solar corona surrounding the Occulter with its camera, which includes the

region that is more than 10 times the solar angular diameter. **Fig. 2** shows the configuration of the two CubeSats while executing the IAH. Specifically, θ_{\odot} denotes the angular diameter of the sun; d and α denote the relative distance and the alignment angle, respectively; T_i ($i = 1, 2, 3, 4$) denotes the direction of the thrust; θ_i ($i = 1, 2$) denotes the orientation of the CubeSats with respect to the sun; and θ denotes the camera's field of view (FOV).

The mission lifetime is six months and comprises three phases: the launch and early orbit phase (LEOP), the drift recovery and station keeping phase (DRSKP), and the autonomous formation flying phase (AFFP). Each phase comprises several modes for monitoring the system status, communication, commissioning hardware, and control utilizing actuators. The two CubeSats typically monitor their status, which includes the current, temperature, position, and angular velocity. To implement formation flying, Pumbaa performs the relative navigation using the navigation data from Timon through the ISL. The DADC technique prevents them from drifting away from each other, while maintaining a relative distance within a few kilometers (Lee et al., 2019).

2.1. Allocation of mission requirements and constraints

Generally, the solar corona's light intensity is extremely low in visible light, which is 10^{-6} times dimmer than the solar photosphere (Romoli et al., 2003). While Timon is placed in the umbra of the Occulter to accomplish the final goal, the FOV shall include the region of interest with the solar corona. The relative distance and alignment angle affect the coverage of the photosphere and corona. Timon's orientation affects the location of the corona image in the focal plane of the camera. The relative distance shall be restricted to less than 5 m for 40 m of the baseline, and the alignment angle shall be less than 7.5° . **Fig. 3** shows images of the solar corona resulting from inaccurate relative positioning and orientation between the two CubeSats.

Table 1 shows the key mission requirements for the orientation and relative positioning. The FOV shall be wider than 30° . The effective area of the Occulter shall exceed

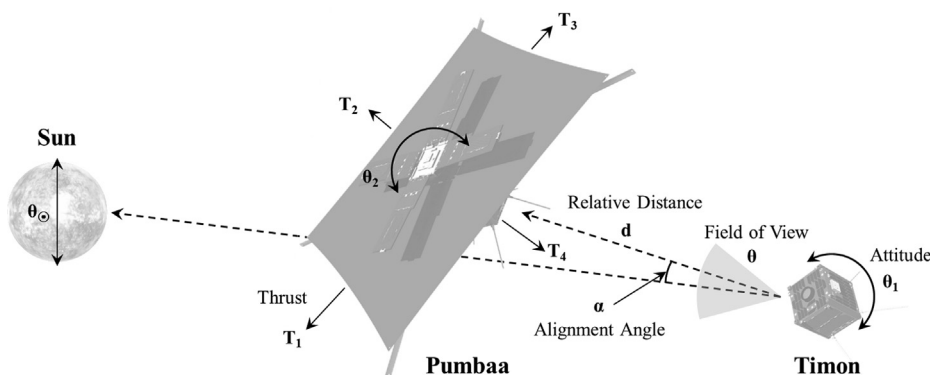


Fig. 2. Configuration of the two CubeSats in the IAH.

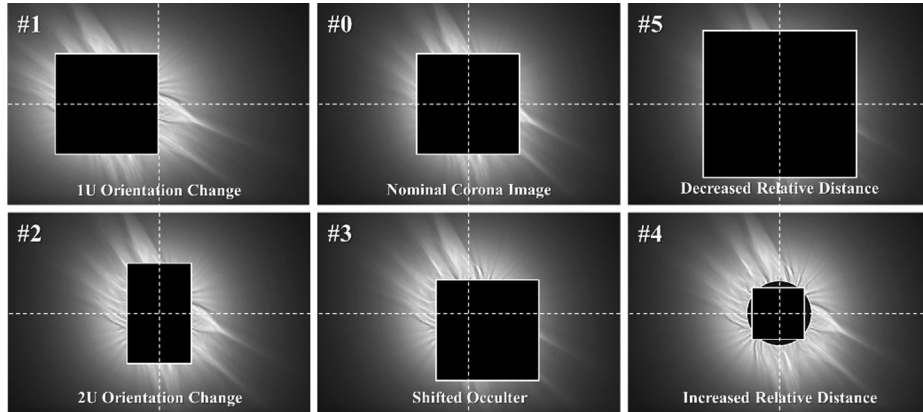


Fig. 3. Expected corona images from Timon's view.

Table 1
Summary of the mission requirements.

Contents	Timon (1U CubeSat)	Pumbaa (2U CubeSat)
Mission Lifetime	> 6 months	
Payload Specifications	> 30.0° (camera FOV) visible light (400–1000 nm)	> 0.5 m × 0.5 m (Occulter size) < $10^{-6} I_{\odot}$ (transmission)
Relative Distance	40.0 m (nominal relative distance) 20.0 (collision avoidance) ~ 53.0 m	
Relative Orbit Control (3σ)	–	< 5.0 m (relative distance) < 7.5° (alignment angle)
Orbit Determination (3σ)	< 50.0 m (absolute, 3D RMS)	< 50.0 m (absolute, 3D RMS) < 1.0 m (relative, each axis)
Attitude Control (3σ)	< 5.0° (Sun pointing error) < 0.5°/sec (each axis)	< 3.0° (Sun pointing error) < 0.5°/sec (each axis)
Attitude Determination (3σ)	< 1.5° (each axis) < 0.15°/sec (each axis)	< 1.5° (each axis) < 0.15°/sec (each axis)

0.50 m × 0.50 m. To block the sunlight fully, the Occulter shall have a single membrane structure that uses a film with a low transmittance.

2.2. Concept of the operations and mission scenarios

2.2.1. Phase I – Launch & early orbit phase (LEOP)

The concept of the operations is shown in Fig. 4, which includes the phases over the mission lifetime. In the LEOP, Timon and Pumbaa are in operations. Following separation from the launch vehicle, they deploy the UHF antenna and start to transmit the beacon signals. Subsequently, they implement B-dot control to stabilize their initial spins by using the three-axis MTQs. Following the detumbling operation, Pumbaa deploys the solar array, and they are oriented toward the sun to maximize the electrical charging. Commissioning operations are carried out via ground-based scheduling to verify the in-orbit availability for each component. First, Timon and Pumbaa operate the GNSS receiver to update the ephemeris and perform the evaluation of the in-orbit performances, which include the power on-off scheduling, the time to first fix, and the navigation solution accuracy. Then, Timon captures several images of Earth and the moon to calibrate the RGB

sensitivity of CMOS sensor on the camera. Pumbaa controls the speed of each wheel on the RWA. Finally, commissioning of the PPS is performed to evaluate and calibrate the conditions of the firing logic, which enables heaters on the propellant tank and each nozzle. Because the physical configurations of the two CubeSats—such as the mass and effective drag area—differ, the distance between them gradually increases to over a few thousand kilometers during the LEOP and commissioning operations.

2.2.2. Phase II – Drift recovery & station-keeping phase (DRSKP)

In the DRSKP, Pumbaa fires its thrusters towards the desired directions, which are determined by the flight dynamics system in the ground segment. Those open-loop maneuvers are repeated until the distance between the CubeSats is reduced to less than 10 km. At the end of the maneuvers, commissioning operations are performed to verify the availability of the ISL and the relative navigation. Finally, when the ISL and the relative navigation are available, the rendezvous maneuver is conducted to satisfy the initial relative states for autonomous formation keeping.

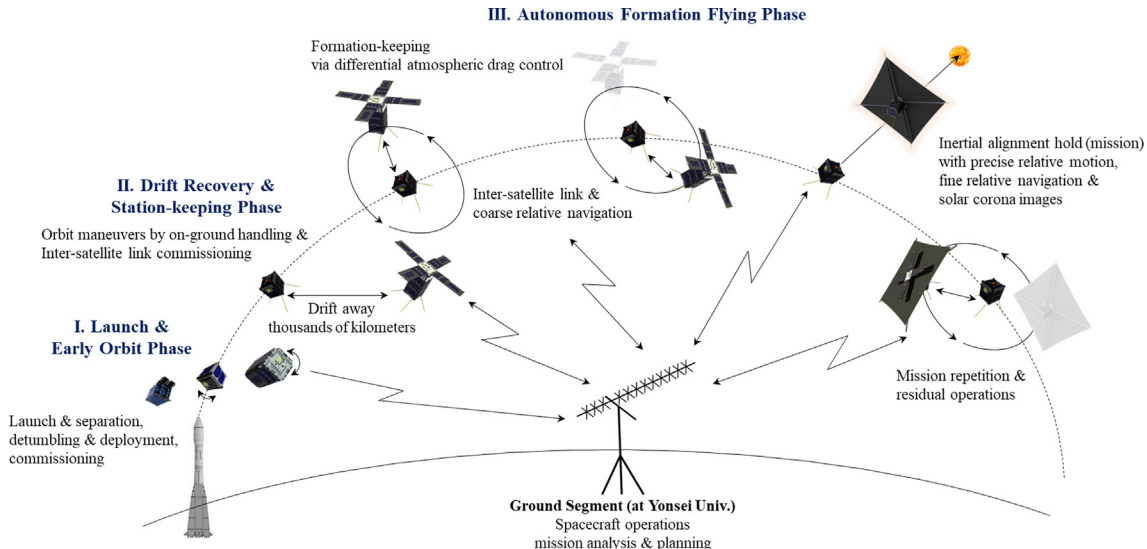


Fig. 4. Concept of the operations for the CANYVAL-C mission.

2.2.3. Phase III – Autonomous formation flying phase (AFFP)

In the AFFP, the relative distance is maintained by executing the DADC technique, which does not require propellant consumptions; Pumbaa changes its orientation toward the orbital velocity direction, which provides control acceleration from the differential atmospheric drag (Kim et al., 2019). For the DADC, a coarse relative navigation with the ISL is carried out by subtracting the navigation solutions between each CubeSat. It is important to determine the available mission schedule, which will be analyzed by the mission analysis and planning software. Immediately prior to the mission operations, Timon begins to be oriented towards the sun. For the IAH, a precise relative positioning is implemented with a fine relative navigation based on the differential GPS (DGPS) algorithm (Leung and Montenbruck, 2005). While Timon is in the artificial eclipse that is given by their precise alignment, the value of the signals from the sun sensor changes. By triggering the signal with predefined values, Timon operates the camera and obtains the images of the corona surrounding the Occulter. After the end of the IAH, the relative distance is maintained within a few kilometers to repeat the mission operations throughout the mission lifetime.

2.2.4. Operation modes

Fig. 5 shows that each phase is composed of several modes, and it describes a flow between each mode. After the end of detumbling in the LEOP, both CubeSats enter the normal mode by the ground telecommand. Basically, the normal, communication, and emergency modes are each autonomously activated by monitoring the system status such as battery voltage level, temperature, ground commanded schedule, etc. In normal mode, each CubeSat stands-by for receiving ground telecommands to

change the mode, monitoring the status and schedule. The downlink of the telemetry and mission data is executed during the communication mode. The emergency mode has the highest priority and handles the contingencies of the systems, for example, sun-pointing for charging battery, detumbling to stabilize body spins, and autonomous execution of back-up scenarios to mitigate effects by a communication fail. The commissioning, control, and mission modes can be entered and implemented via ground telecommands. Specially, the control mode includes the attitude pointing and orbit control. The mission mode is defined as the mode for the mission operations including the relative navigation and orbit control. When the operations of each mode are completed, the CubeSats are back to the normal mode automatically.

3. CubeSat system design for autonomous formation flying

The two CubeSat systems for the CANYVAL-C mission carry the payload and bus. Considering the restricted internal space, several components were integrated for a miniaturization and the electrical interfaces were designed to reduce the wiring.

Timon is equipped with a visible camera as the main payload, and its attitude is controlled by using only the MTQ in each axis. The UHF transceiver and the GNSS receiver are mounted on the OBC as a space-saving design. The Pumbaa's components for the sensors, CNDH, and COMS are the same as those of Timon's. Specially, the RWA and PPS that are based on a cold gas thruster are included, which provides accurate and rapid attitude control and positioning maneuvers, respectively. With four deployable solar panels, the EPS enhances the electrical power capabilities.

Fig. 6 shows the internal and external configurations of Timon and Pumbaa. Table 2 lists the components of each

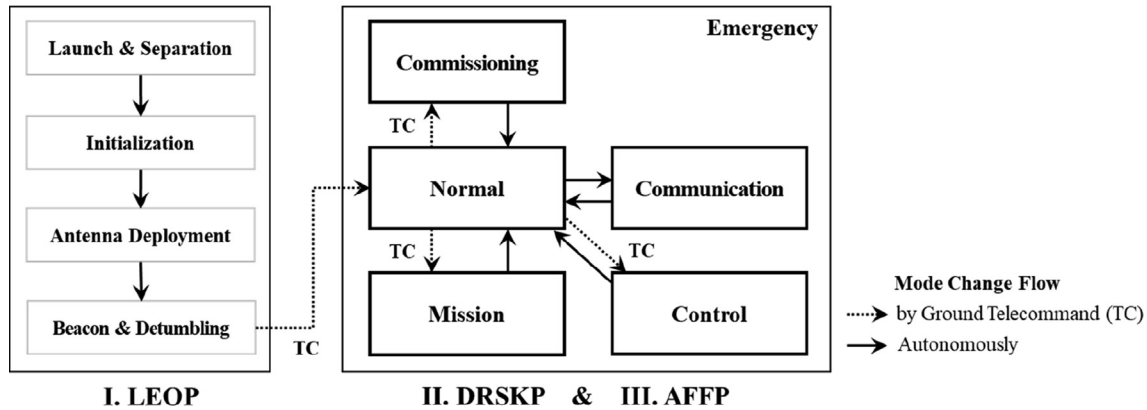


Fig. 5. Flowchart of the operation modes.

CubeSat based on the manufacturers. Most of the subsystems are constructed with COTS. The systems are developed in accordance with the proto-flight model philosophy.

3.1. Payload design

Following the aforementioned requirements and constraints, NanoCam C1U is suitable as the payload of Timon, and a black-colored polyimide film is applied to the Occulter. Fig. 7 shows the configuration of each payload.

Timon's payload consists of a space-proven COTS detector and optics (GomSpace, 2020a). The ½-inch format color CMOS sensor has a resolution of 2048×1536 pixels with a 10-bit RGGB Bayer pattern. The optics include Schneider Kreuznach's commercial lens. The focal length of the lens is 8.2 mm, the f-number is 1.4, and it covers a wide area ($33.4^\circ \times 44.5^\circ$ of the FOV).

Given the size of the RWA and PPS, only small internal spaces are allowed in components of Pumbaa. The Occulter shall be miniaturized so that it is smaller than 0.5U, which consists of a film storage and a deployment mechanism. The thin black polyimide film from SKC Kolon Corp. has low reactivity in thermal environments and extremely low transmittance in visible light (SKC Kolon PI, 2020). The deployed film has a single membrane configuration to prevent the transmittance of sunlight. By modifying the Miura-ori folding method (Fu et al., 2016), the film is folded within 0.3U, and the film walls and hinges store the folded film before deployment. Four steel tape measures spread the stowed film so that it has a size of about $0.75 \text{ m} \times 0.75 \text{ m}$ and the mechanism is based on the solar sail (Song, 2016). The HRM electrical board is attached to the top side of the Occulter, which enables the deployment of the film walls and tape measures.

3.2. Bus design

As can be seen from the illustrations of the electrical interfaces in Fig. 8, the bus architectures of Timon and Pumbaa are similar. The electrical interfaces for the power

supply and data communication are connected using PC104, board-to-board, and RF cables. With two-wire electrical interfaces such as CAN and I²C for the main data communication, the amount of wiring was significantly reduced compared to SPI or UART. Unlike Timon, Pumbaa is equipped with RWA and PPS supporting I²C and CAN, respectively. In addition, the deployment devices for the Occulter and solar array are attached to Pumbaa.

The OBC handles the data communication and electrical power interfaces, and support the CAN, I²C, and UART interfaces for telemetry and telecommand. The OBC redistributes the electrical power to each component; the electrical power is provided by the power control and distribution unit (PCDU). The main attitude sensors are applied to the fine sun sensor, the magnetometer (MMT), and the inertial measurement unit (IMU); the MMT and IMU are embedded on the OBC. The GNSS receiver, which is termed OEM719, is used for on-board navigation and obtains its position and velocity. The UHF transceiver (the NanoCom AX100U) is utilized and it supports in-orbit reconfiguration of the parameters such as the baud rate and main frequency. This functionality enables uplink, downlink, and ISL with a single transceiver.

Before the launch and operations are in orbit, two kill switches deactivate the PCDU to prevent a battery discharge. The analog signal from the photodiode is converted to an I²C digital output on each solar panel, which reduces the electrical harnesses. The battery bus voltage is regulated to 3.3 V, 5.0 V, and 12.0 V bus voltages by the PCDU. The latch-up switches on the PCDU protect other components from overcurrent and it enables electrical power management. In addition, the PCDU includes the functionalities of the maximum power point tracker and the end of charging on the battery charge regulator, which handles the solar array input and battery charging.

3.2.1. Attitude and orbit control subsystem (AOCS)

The attitude sensors for the CubeSats consist of a coarse sun sensor (CSS), the fine sun sensor (FSS), the MMT, and the IMU. The 3-axis MTQs are for both CubeSats. The

Table 2
Components of the subsystems.

(a) Timon (1U CubeSat)			
Subsystem	Components	Models	Remarks
Payload	Camera	GomSpace, NanoCam C1U-8	Visible light, 400–1000 nm
AOCS	Inertial Measurement Unit Magnetometer Analog Sun Sensor Magnetic Torquer	InvenSense, ICM-20689 MEMSIC, MMC5883MA SolarMEMS, nanoSSOC-A60 In-house, air coil	3-axis accelerometer, gyro 3-axis $< 0.5^\circ$ accuracy $< 0.1 \text{ Am}^2$ in each axis
CNDH	On-board Computer	Nara Space Tech., AT91SAM9X25	$< 400 \text{ MHz}$ clock speed
COMS	UHF Transceiver UHF Antenna	GomSpace, NanoCom AX100U GomSpace, NanoCom ANT430	Software Defined Radio Omnidirectional
EPS	Power Distribution and Control Unit Battery Large Solar Cell Array Small Solar Cell Array 1 Small Solar Cell Array 2 Kill Switch	Clyde Space, 25-02451 Clyde Space, 01-02685 (Integrated 20 Wh) Azur Space, 30% triple junction GaAs TrisolX, 28% triple junction GaAs TrisolX, 28% triple junction GaAs Panasonic, AV404461	SEPIC (4ch) 3.7 V Li-polymer, 2S-2P 2S-1P (+X, -X, -Y, +Z) 2S-10P (+Y) 2S-11P (-Z) 2 EA
SMS	Frame Separation Spring	In-house, 1U MISUMI, SPJY4	Al6061 (anodized) 4 EA
(b) Pumbaa (2U CubeSat)			
Subsystem	Components	Models	Remarks
Payload	Occulter	In-house, 0.5U (Stowed)	$0.75 \times 0.75 \text{ m}^2$ (Deployed)
AOCS	Inertial Measurement Unit Magnetometer Digital Sun Sensor Digital Sun Sensor Magnetic Torquer Reaction Wheel Assembly Propulsion system	InvenSense, ICM-20689 MEMSIC, MMC5883MA SolarMEMS, nanoSSOC-D60 Nara Space Tech., NST DSS In-house, air coil Clyde Space, 3-axis Standalone GomSpace, MEMS cold gas thruster	3-axis accelerometer, gyro 3-axis $< 0.5^\circ$ accuracy $< 1.5^\circ$ accuracy $< 0.1 \text{ Am}^2$ in each axis $< 0.23 \text{ mNm}, 3.53 \text{ mNm}$ $< 1 \text{ mN}, 40 \text{ Ns}$ (Butane)
CNDH	On-board Computer	Nara Space Tech., AT91SAM9X25	$< 400 \text{ MHz}$ clock speed
COMS	UHF Transceiver UHF Antenna	GomSpace, NanoCom AX100U GomSpace, NanoCom ANT430	Software Defined Radio Omnidirectional
EPS	Power Distribution and Control Unit Battery Deployable Solar Cell Array Body-mount Solar Cell Array 1 Body-mount Solar Cell Array 2 Kill Switch	Clyde Space, 25-02452 Clyde Space, 01-02685 (Standalone 30 Wh) Azur Space, 30% triple junction GaAs Azur Space, 30% triple junction GaAs Azur Space, 30% triple junction GaAs Panasonic, AV404461	BUCK (2ch), SEPIC (1ch) 3.7 V Li-polymer, 2S-3P 6S-2P (-Z) 3S-1P (+X, -X, +Y, -Y) 2S-1P (+Z) 2 EA
SMS	Frame Hold-and-release Mechanism (HRM) Separation Spring	In-house, 1.5U SoleTop / Chosun Univ., Hinge Deployment MISUMI, SPJY4	Al6061 (anodized) Solar Array, Occulter 4 EA

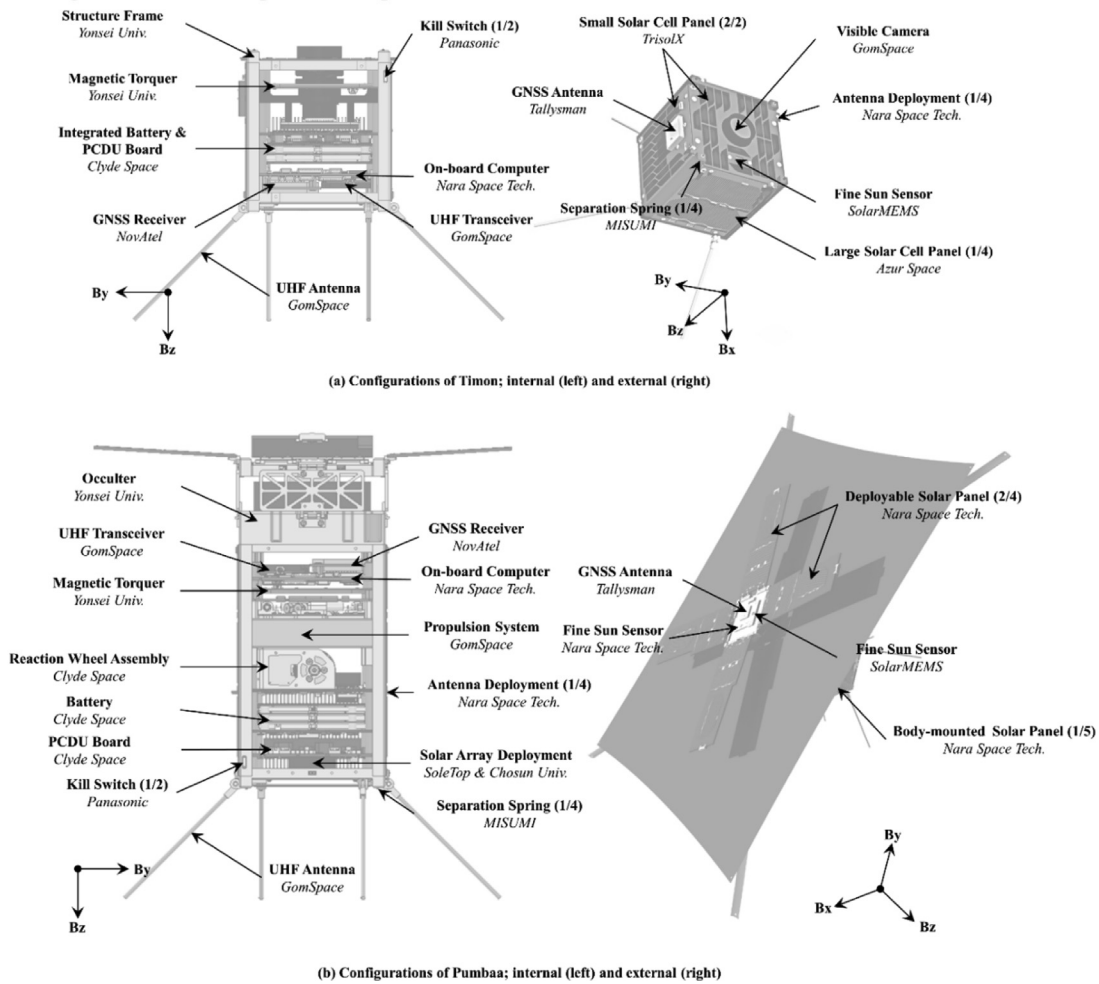


Fig. 6. Configurations and component composition; (a) Timon (1U CubeSat), (b) Pumbaa (2U CubeSat).

RWA and PPS are only for Pumbaa. Fig. 9 shows the actuators of the AOCS.

The CSS comprises several photodiodes attached to each body-mounted panel. The attitude is determined in real time by using an extended Kalman filter (EKF). The sensors used for navigation are chosen according to the operating environment and the details of the determination algorithm that changes over the selected sensors. While placed in the eclipse, the CubeSats propagate the last states only for the attitude estimation. The initial attitude knowledge applied to the EKF as an initial state vector is obtained by the TRIAD method, which forms the transformation matrix by using the sun vector and the Earth magnetic vector.

For practical reasons such as the structural constraint and power capacity, Timon maneuvers its attitude using 3-axis air-coil-type MTQs, which consume less than 0.5 W per unit. The attitude control algorithm is changed according to the actuator. The MTQs control the attitude by interacting with Earth's magnetic field. The performance of the MTQ is dependent on the direction and magnitude of Earth's magnetic vector. The sliding mode

control is applied to compensate for the nonlinearity caused by the disturbance. On the other hand, the Pumbaa controls its attitude with the PID controller as the RWA is able to generate higher torque, which guarantees a pointing accuracy within 3.0°.

With the attitude actuators and sensors, Timon and Pumbaa can perform pointing maneuvers within a few degrees in daylight. The attitude control and determination are executed with time-sharing to avoid estimation errors due to the effect of the MTQ's magnetic field on the MMT. Only Pumbaa has the capability of orbit maneuvers with the PPS. The relative navigation is divided into two modes, namely, coarse mode and fine mode. The coarse mode for the DADC is accomplished by substituting Pumbaa's navigation solution with Timon's, which cancels the effects caused by an ionosphere (Roth, 2010). The fine mode is implemented to achieve precise relative orbit maneuvers using the GNSS measurement data from the GPS L1 and GLONASS signals. Timon transmits the data to Pumbaa every 5 s via the ISL. Then, Pumbaa executes the algorithm that is based on the DGPS, which improves the performance by eliminating errors from the clock of the

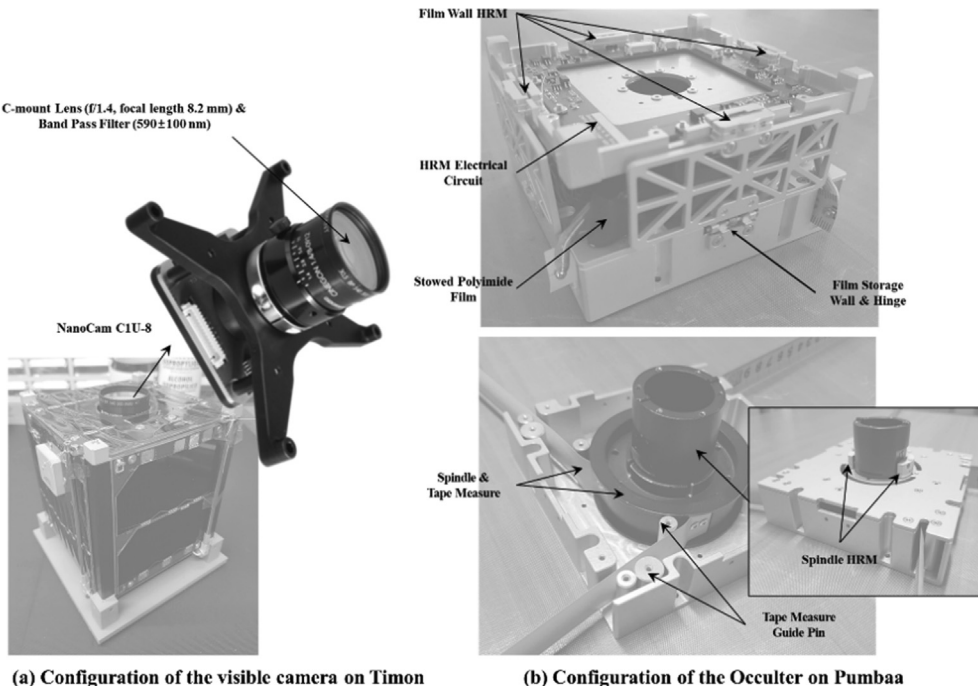


Fig. 7. Configuration of each payload; (a) NanoCam C1U, (b) Occulter.

GNSS satellite, the receiver, and the noise terms (Misra and Enge, 2011). In addition, for the mission mode, the GNSS antennas of Pumbaa and Timon point in different directions with a difference of 90° owing to a structural constraint. This makes the visibility of the GNSS satellites low, and eventually the relative navigation fails. To mitigate the constraints in the visibility, Timon orients its GNSS antenna close to the zenith (Lee et al., 2021).

Fig. 10 illustrates a general diagram of functions and their flow among the orbit and attitude control, wherein chief and deputy mean Timon and Pumbaa, respectively. The control loop for the formation flying is related to the navigation and orbit control functions, which generates the desired trajectory by estimating the relative states. The orbit controller calculates the force vector determining a target quaternion. After aligning the orientation of Pumbaa with the target using the attitude controller and actuators, the selected thrusters are activated. As the relative navigation has a loop of 5 s, the entire control loop is 10 s, including the 5 s for firing thrusters. For the DADC, only the attitude actuators are activated to change and maintain the desired orientations.

3.2.2. Propulsion system (PPS)

The PPS on Pumbaa is of cold gas type and it provides a maximum thrust of 1 mN (GomSpace, 2020b). The model is customized to provide two 2D thrusts, in which the x- and y-axes are along the body frame with four MEMS thruster nozzles. The nominal thrust is an impulse of 1 mN with a pulse width of 10 ms, which enables a continuous thrust. Given a propellant budget of 15 m/s during the mission lifetime, the capability of the propellant storage is

up to 45 Ns for compressed butane. The propellant tank is manufactured by 3D printing titanium alloy and it is miniaturized to be less than 0.4U. The configuration of the PPS is shown in Fig. 9 (c).

3.2.3. Command and data handling subsystem (CNDH)

The OBC has the following capabilities and features: low power consumption within 0.5 W, 400 MHz clock speed with the ARM cortex A9, embedded Linux OS, docking the UHF transceiver, the GNSS receiver in a single board, and ability to act as an interface board. From the total ionizing doze (TID) testing, this study verified that the OBC can endure space radiation environment up to 27 krad, which the value is accumulated over three years in low Earth orbit. Fig. 11 displays the mechanical configuration of the OBC.

The FSW is based on the cFS, which is used as the main platform for the FSW; thus, the FSW has a simplified architecture and is robust in terms of multi-tasking, including the computation of the AOCS algorithms. With the basic functions in the cFS, the software bus (SB) provides the interface among each module, which enhances the robustness of the FSW and reduces the development cost. The architecture of the FSW is presented in Fig. 12.

3.2.4. Communication subsystem (COMS)

The UHF transceiver, which is based on software-defined radio (SDR), enables the ISL, uplink, and down-link with a single on-board communication device by having main frequencies of 436.330 MHz and 437.500 MHz for each CubeSat. A guide band at 50 kHz prevents RF interference between the two CubeSats. Given the link budget,

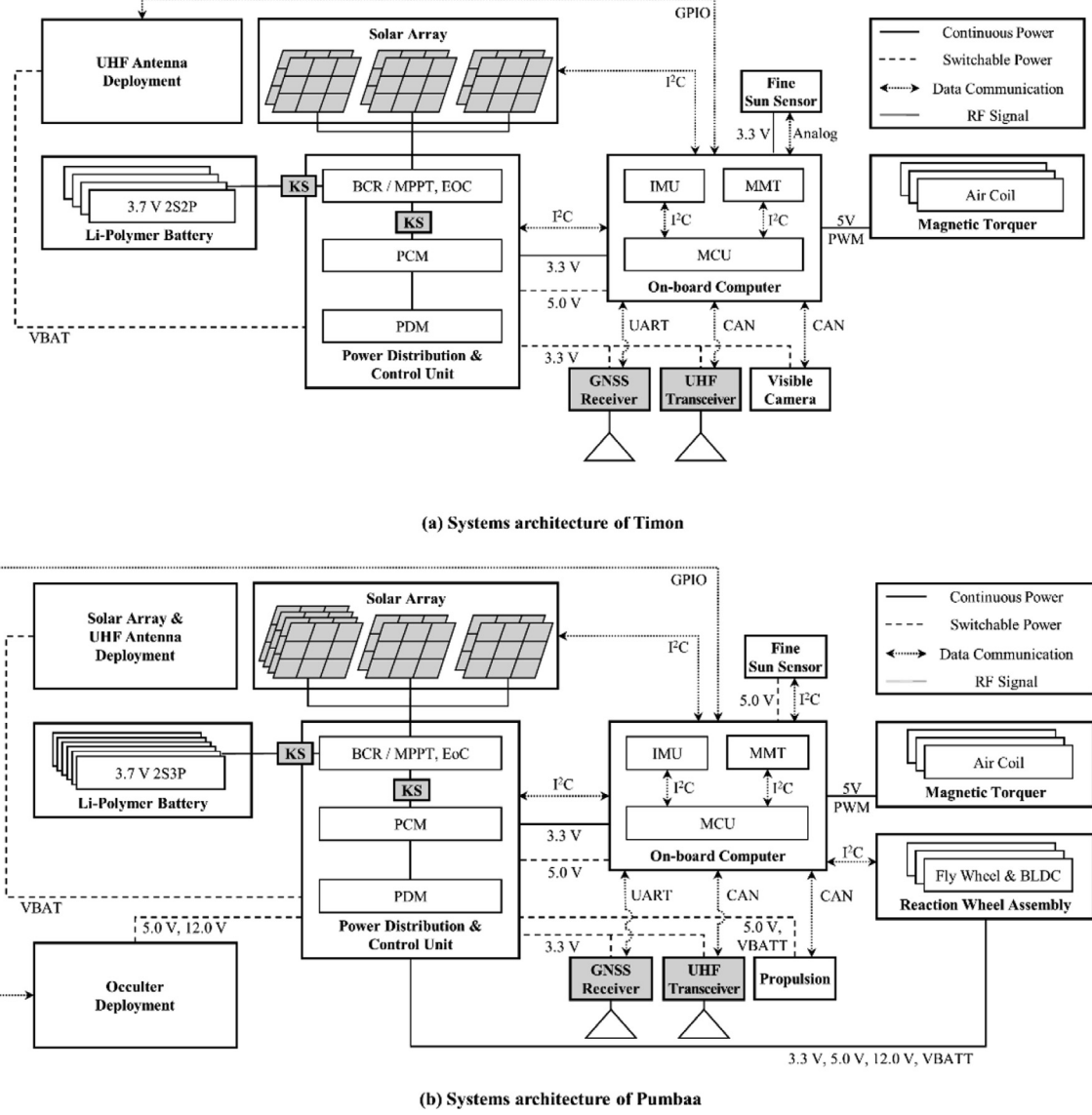


Fig. 8. Systems architecture; (a) Timon (1U CubeSat), (b) Pumbaa (2U CubeSat).

the baud rate was set to 9.6 kbps for the downlink and the ISL, and 4.8 kbps for the uplink. While performing the ISL for the relative navigation, Timon changes its main frequency to match that of Pumbaa. Integrity checks are performed periodically. The protocol corresponds to the ASM and Golay, and the modulation to the GFSK. Circular polarization with an omnidirectional antenna enhances the capability of the uplink and downlink. Fig. 13 shows the configurations of the RF communication subsystem.

3.2.5. Electrical power subsystem (EPS)

Timon has six body-mounted solar panels with highly efficient triple-junction GaAs cells on each axis, as illustrated in Fig. 6 (a). The remaining areas of the GNSS antenna or the camera side panels are filled with small cells from the TrisolX to maximize power generation. Pumbaa has five body-mounted solar panels and four deployable solar panels with triple-junction GaAs cells, as depicted

in Fig. 6 (b). The body-mounted solar panels are connected to the SEPIC BCR, and the deployable solar panels are connected to the BUCK BCR. The fractional open circuit voltage method is applied to each BCR and it guarantees a conversion efficiency higher than 90%. At the end of life, the orbit average power generation with sun-pointing is up to 2.0 W for Timon and 8.3 W for Pumbaa, respectively.

To keep the positive electrical power margin in the normal mode, the GNSS receiver can operate for only a few minutes in daylight. The GNSS receiver is turned on for less than 30 min in every orbital period, and the DADC and coarse relative navigation are implemented during those periods. Timon and Pumbaa have 3.7 V Li-polymer battery arrays with 20 Wh and 30 Wh capacities, respectively. With the duty-cycled operation strategy and the selected battery capacity, the depth of discharge for each CubeSat is within 50% for the mission operations, and it is normally within 20%, assuring the systems lifetime.

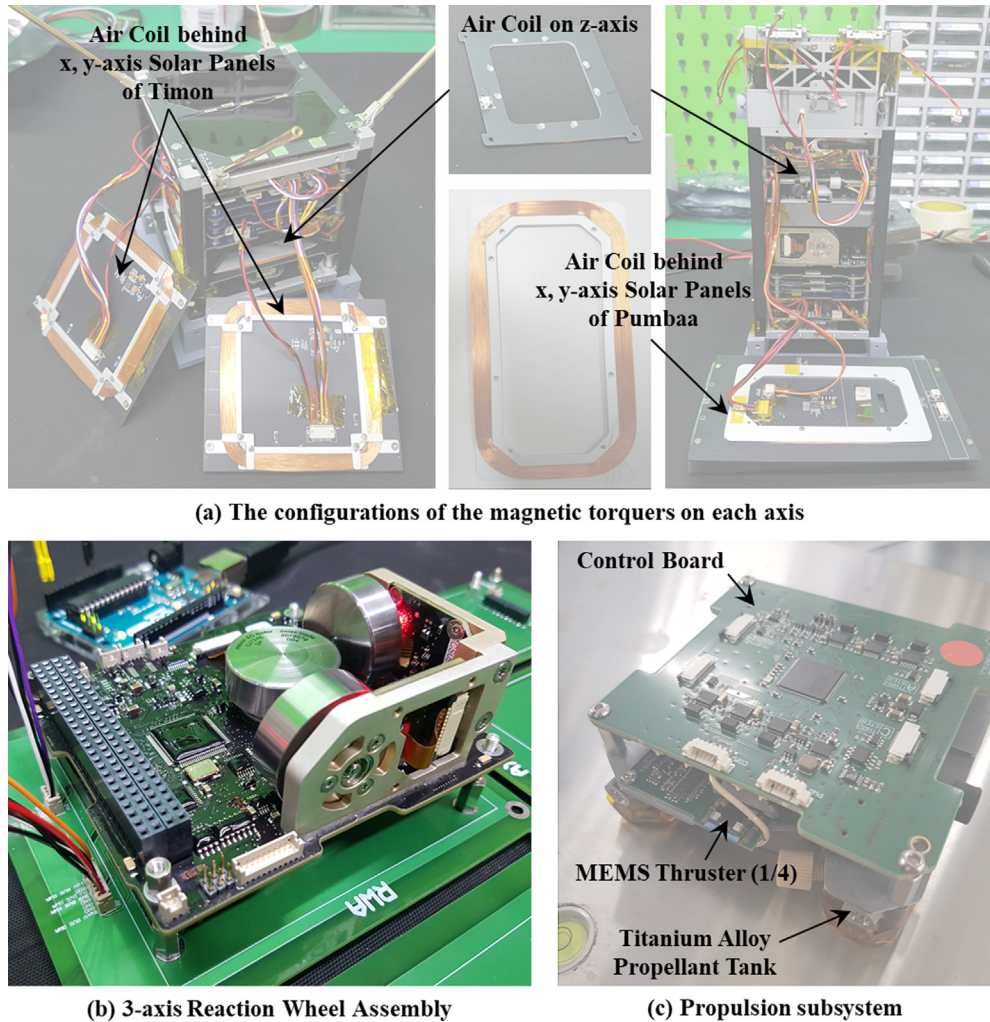


Fig. 9. Configuration of the actuators; (a) MTQ, (b) RWA, (c) PPS.

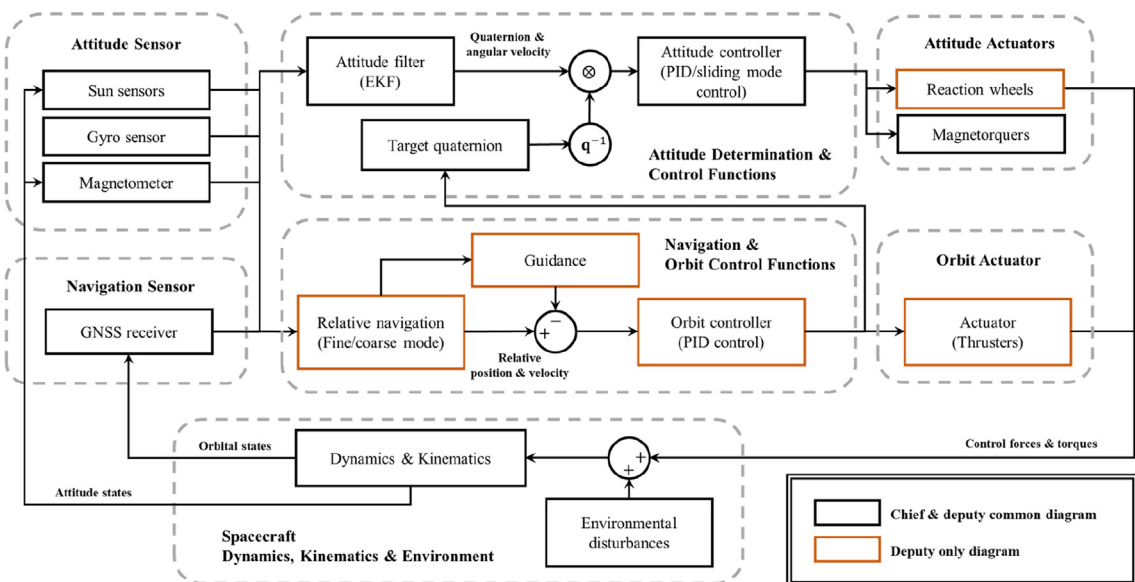


Fig. 10. Diagram of the attitude and orbit control loop for the formation flying.

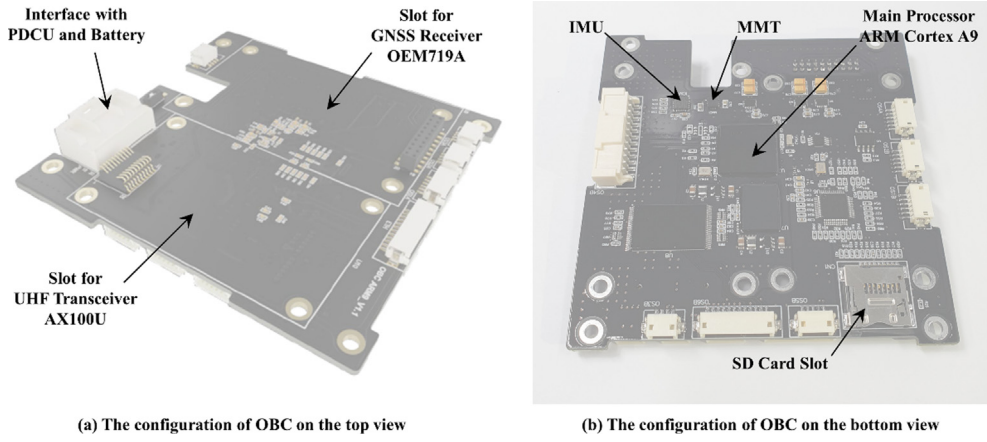


Fig. 11. Configuration of the OBC; (a) top view, (b) bottom view.

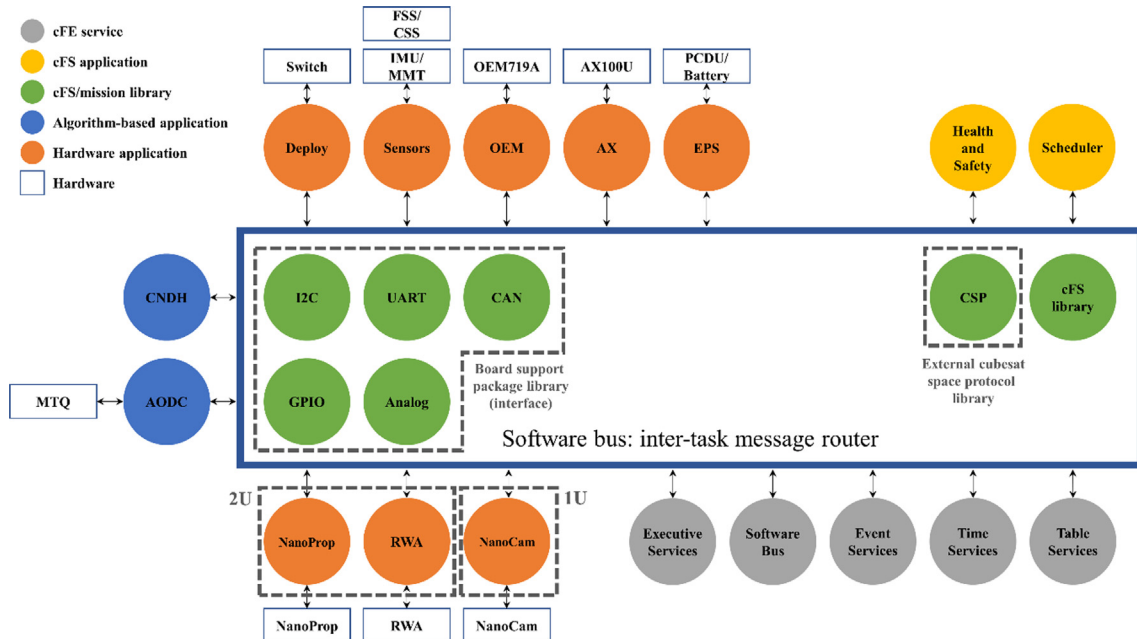


Fig. 12. Architecture of the cFS based FSW.

3.2.6. Structure and mechanism subsystem (SMS)

Most of the structural parts, including the frame and hinge mechanism, are constructed with aluminum 6061 alloy. The surfaces of these parts are anodized to prevent cold welding between the CubeSat deployer (Cho et al., 2019). The frames with a skeleton configuration have a high degree of freedom in the assembly. Given the internal space, thin aluminum plates are attached to the body-mounted solar panels as brackets for each MTQ. These function as stiffeners (Fig. 9 (a)). From the simulation with the NX10.0 NASTRAN, the first mode frequency (f_0) is analyzed above 150 Hz and it is sufficiently higher than the recommended value to avoid resonance with a launch vehicle.

The radiation shielding is assured by the FR-4 PCB of the body-mounted solar panel with a thickness of 1.2 mm. The TID of the internal components is approxi-

mately 6.83 krad over 1 year, which was analyzed by the SPENVIS SHILDOSE-2 model (SPENVIS, 2020).

The hinge mechanism includes the torsion springs and stopper structure, and it deploys the solar panels and film storage walls of Pumbaa. All deployments are implemented by melting a nylon wire that holds the UHF antenna, solar panels, and film storage walls.

3.2.7. Thermal control subsystem (TCS)

Passive thermal control is applied to each CubeSat by using an anodized aluminum frame and a black FR-4 PCB. The battery board includes the heater for heat dissipations, which maintains the temperature of the battery cells so that they are above 0 °C. The thermal transient simulation was conducted with NX10.0 Space Thermal Systems. The temperature range is within the operating temperature, while the deactivated components are within

the survival temperature, which are above 10 °C of the thermal margins.

4. Systems analysis for mission assurance

4.1. Prerequisite for mission assurance

While performing the IAH to obtain the images of the solar corona, Timon and Pumbaa shall maintain the required relative distance and minimize the alignment angle simultaneously. However, in practical cases, because of systems limitations, such as the thrust magnitude and the torque provided by the RWA, it is difficult to meet these ideal requirements. The implementation of the IAH is divided into three cases. The first case needs to meet the requirements for the relative distance only, the second case is the alignment angle only, and the third case is to satisfy both requirements. In this study, the system analysis utilizes only the third case to accomplish the final mission goal.

4.2. Attitude and orbit analysis

Numerical simulations were conducted to evaluate the AOCS performance for the mission assurance. The orbit parameters were assumed to be the sun synchronous orbit with a 500 km altitude and it was the local time on the ascending node of 11:00:000.00. The simulations considered the characteristics of the sensors and actuators.

The simulations are carried out in three steps. First, the attitude determination and control algorithms are verified given the pointing scenarios including sun-pointing and nadir-pointing over several periods. Then, the relative navigation algorithms for the coarse and fine mode are verified by the HILS according to the relative orbit control scenarios including the DADC, rendezvous, and IAH. Finally, the performances of the integrated attitude and orbit control algorithms with execution strategy of sensors and actuators are evaluated through the Monte Carlo simulation to assure the feasibility of the orbit control scenarios including the DRSK, DADC, rendezvous, and IAH. This paper particularly deals with only the IAH, which is relevant to the final mission goal.

4.2.1. Step I – Attitude determination and control

To carry out the mission, as presented in Fig. 2, the camera on Timon is oriented to the sun, and the Occulter on Pumbaa is perpendicular to the sun within 5.0° and 3.0° in 3-sigma, respectively. Uncertainty in the geomagnetic field makes the sun-pointing error of Timon greater than Pumbaa, inducing peak values which exceed 5.0°. According to the simulations, the pointing errors of Timon and Pumbaa are reduced below the thresholds within three orbital periods from any initial state, as demonstrated in Fig. 14. Because of the artificial eclipse due to the inertial alignment, the pointing error of Timon is not ruined much, as presented in Fig. 14 (a). To mitigate the degradation of

an image quality with the instantaneous pointing error, Timon attempts to take multiple images in a short time when the artificial eclipse is established.

4.2.2. Step II – Relative navigation

The relative navigation algorithms are evaluated with the HILS, which uses GNSS signal generator, GNSS receiver, and the systems for trajectory generation (Lee et al., 2021). The reference trajectories for the rendezvous and IAH scenarios, which utilize the PPS, are generated prior to the simulations. To consider the effects of the GNSS antenna characteristics, the orientation and thrusts, the controlled attitude and orbit profiles of the CubeSats for each scenario are applied to the simulations. The performance according to the requirements is presented in Table 3. The coarse mode for the DADC can estimate Pumbaa's relative position within 10 m in each axis, using the navigation solutions provided by the GNSS receivers on each CubeSat. The fine mode for the rendezvous and the IAH can estimate the relative position within 50 cm for each axis, considering the feedback of the thrusts. The results meet the assigned requirements in 3-sigma.

4.2.3. Step III – Integrated attitude and orbit control

Coupled attitude-orbit dynamics are considered for the analysis of the fidelity in the IAH by integrating the attitude and orbit control algorithms of both CubeSats. In addition, the structural features, which schedule the execution of the actuators and sensors, and the physical characteristics of the actuators were also modeled for the simulations. For example, the thrust errors induced by the misalignment and the magnitude are assumed to be 1° and 5% for 1σ, respectively. The relative navigation errors are randomly applied as 1 m and 0.1 m/s in each axis for 3σ. Prior to the simulations, the available initial states for the IAH success have been analyzed considering only orbit control algorithm according to the operation orbit, dynamic models, and error sources from the physical property of CubeSats. The results are depending on the initial states, specially, on along-track direction. The initial position should be constrained within ± 120 m for the along-track. As shown in Fig. 15 and Table 4 for 100 times the Monte Carlo simulation, the IAH is feasible with the developed AOCS; the upper figure shows state profiles of a single case, and the bottom figure shows the results of the Monte Carlo simulation given samples with various initial states. The control error of the relative distance is within 3 m, and the alignment angle is within 5°, which meets the requirements. The alignment duration exceeds 6 min, which consumes approximately 5 Ns for every attempt. The propellant margin is sufficient to implement the orbit maneuvers for more than five times the IAH, which includes several times for the DRSK and rendezvous.

Table 5 shows the estimated propellant consumptions for each orbit control scenario. The accumulated impulses in the DRSKP are significantly less than the others because these maneuvers are established for a long duration with

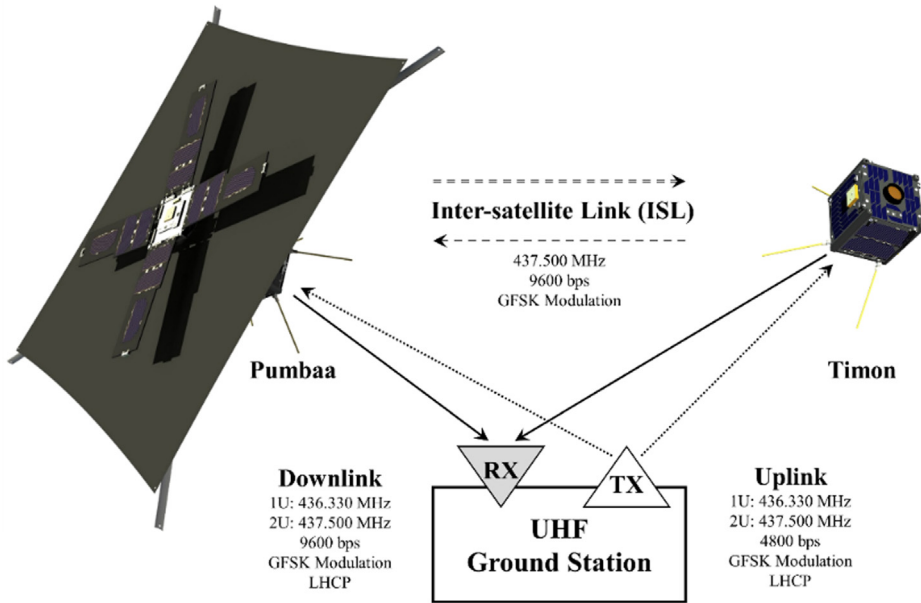


Fig. 13. Configuration of the RF communication subsystem.

several finite burns. On the other hand, the rendezvous and the IAH should be finished within a few orbital periods, consuming much propellant in short time.

4.3. Energy-balancing analysis

The discharging and charging of the battery capacity are balanced by the duty cycled operations of the subsystems and the sun-pointing in the normal mode. The numerical simulation considers the conversion efficiency and numerical models of the photovoltaic cells and Li-polymer battery cells (Villalva et al., 2009; Gao and Liu, 2002). Fig. 16 shows the energy-balancing simulation results for each CubeSat in normal mode and mission mode for five orbital periods. The first subplot of each figure is the power generation, the second is the duty-cycled operations, and the remainder are the battery's state of charge (SOC). In the mission operations, most subsystems are activated and the SOC is decreased to approximately 30% and 7.4 V at the voltage level. To extend the mission lifetime, they shall maintain the sun-pointing after the mission operations, charging the SOC to 70% and 7.7 V at the voltage level.

5. Systems assembly, integration, and verification

5.1. CubeSat assembly and integration

Before the systems assembly, sub-assemblies that include the MTQ in 3-axis, the OBC with the UHF transceiver and the GNSS receiver, and the Occulter were performed. The internal and external configurations of Timon and Pumbaa are presented in Fig. 17. As illustrated in Fig. 17 (a) and (b), the components are stacked, they close the body-mounted solar panels, and hold the deploy-

able solar panels and the UHF antenna with nylon wire. With the assembly sequence, the FSW was integrated onto the OBC and it performed functional testing.

5.2. End-to-end testing

Before the assembly and integration, flat-sat testing with an electrical testbed (ETB) was conducted to verify the interface between the subsystems and functionalities. After the integration, the end-to-end testing was performed and evaluated by the simplified ground segment, as shown in Fig. 18. The system anomalies were checked through real-time operations over one day, demonstrating the telemetry downlink and the telecommand uplink in-orbit operations. The mode changes as the exact schedule are implemented via the telecommand uplink. The real-time and sequential operations following the scenarios on the FSW are executed well without any malfunction.

5.3. Environmental testing

5.3.1. Vibration testing

The structural stiffness and systems robustness of the launch environment were verified through vibration testing. This study verified that the bus of Timon and Pumbaa can endure a high acceleration and extreme vibrations by the launch vehicle, Soyuz-2.1a with the Fregat. The detailed specifications of the vibration testing from the launch provider, Innovative Space Logistics (van Bolhuis et al., 2020), can be found. The low level sine-sweep testing was conducted to identify the natural frequency of the systems and to detect structural changes between each test. The sine burst testing was performed to verify the effect of the quasi-static acceleration load. A random vibration

Table 3

Simulation results of the relative navigation.

Mode	State	Requirements	Radial (mean, 3σ)	In-track (mean, 3σ)	Cross-track (mean, 3σ)
Coarse (DADC)	Position (m, 3σ)	< 60.0 m (each axis)	2.14 ± 3.96	1.47 ± 3.31	2.35 ± 5.66
	Velocity (m/s, 3σ)	< 0.6 m/s (each axis)	0.02 ± 0.04	0.02 ± 0.03	0.03 ± 0.06
Fine (Rendezvous & IAH)	Position (m, 3σ)	< 1.0 m (each axis)	-0.01 ± 0.24	-0.02 ± 0.42	-0.01 ± 0.39
	Velocity (m/s, 3σ)	< 0.01 m/s (each axis)	0.00 ± 0.01	0.00 ± 0.01	0.00 ± 0.01

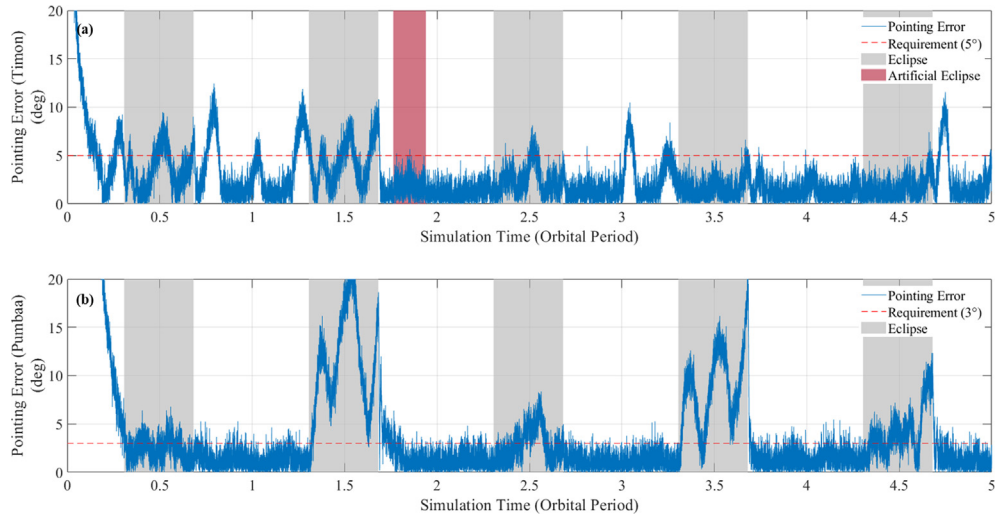


Fig. 14. Profiles of the sun-pointing error; (a) Timon (1U CubeSat), (b) Pumbaa (2U CubeSat).

Table 4

Results of the IAH for 100 times the Monte Carlo simulation.

State	Radial	In-track	Cross-track	Total Impulse (Ns) (mean, 1σ)	Duration (min) (mean, 1σ)
Relative Position (m) (mean, 3σ)	1.57 ± 0.71	1.96 ± 1.04	0.94 ± 1.38	4.09 ± 0.90	9.28 ± 3.17
Relative Distance (m) (mean, 3σ)	1.54 ± 1.28	(with the nominal distance, 40 m)			
Alignment Angle ($^{\circ}$) (mean, 3σ)	4.16 ± 1.14				

Table 5

Propellant budget analysis for each orbit control scenarios.

	Allocated Budget (Ns)	Impulse (Ns)	Max. Attempts (times)	Accumulated Impulse (Ns)	Margin (%)
Drift Recovery	1.0	0.1876	4	0.7504	24.96
Station-keeping	1.0	0.1796	4	0.7184	28.16
Rendezvous	6.0	0.9211	5	4.6055	23.24
IAH	32.0	4.9942	5	24.9710	21.97
Total Accumulated Impulse (Ns)	40.0	—	—	31.0453	22.39

profile was applied to the launch vehicle. The profiles of each testing were set to the proto-flight model.

The testing was performed in the Korea Testing Laboratory. Fig. 19 displays the configurations of the vibration testing set-up. Vibration testing was implemented while Timon and Pumbaa were stowed in a single deployer. Generally, their rails on the frame were constrained by the

deployer, and they could move in the direction of the separation described in the z-axis of the body frame. The 3-axis acceleration sensors were attached to the x- and y-axes deployable solar panels, the z-axis structural frame, and the deployer as a reference.

In Fig. 20, the solid and dashed lines show the profiles of f_0 that were measured at the beginning and end of the

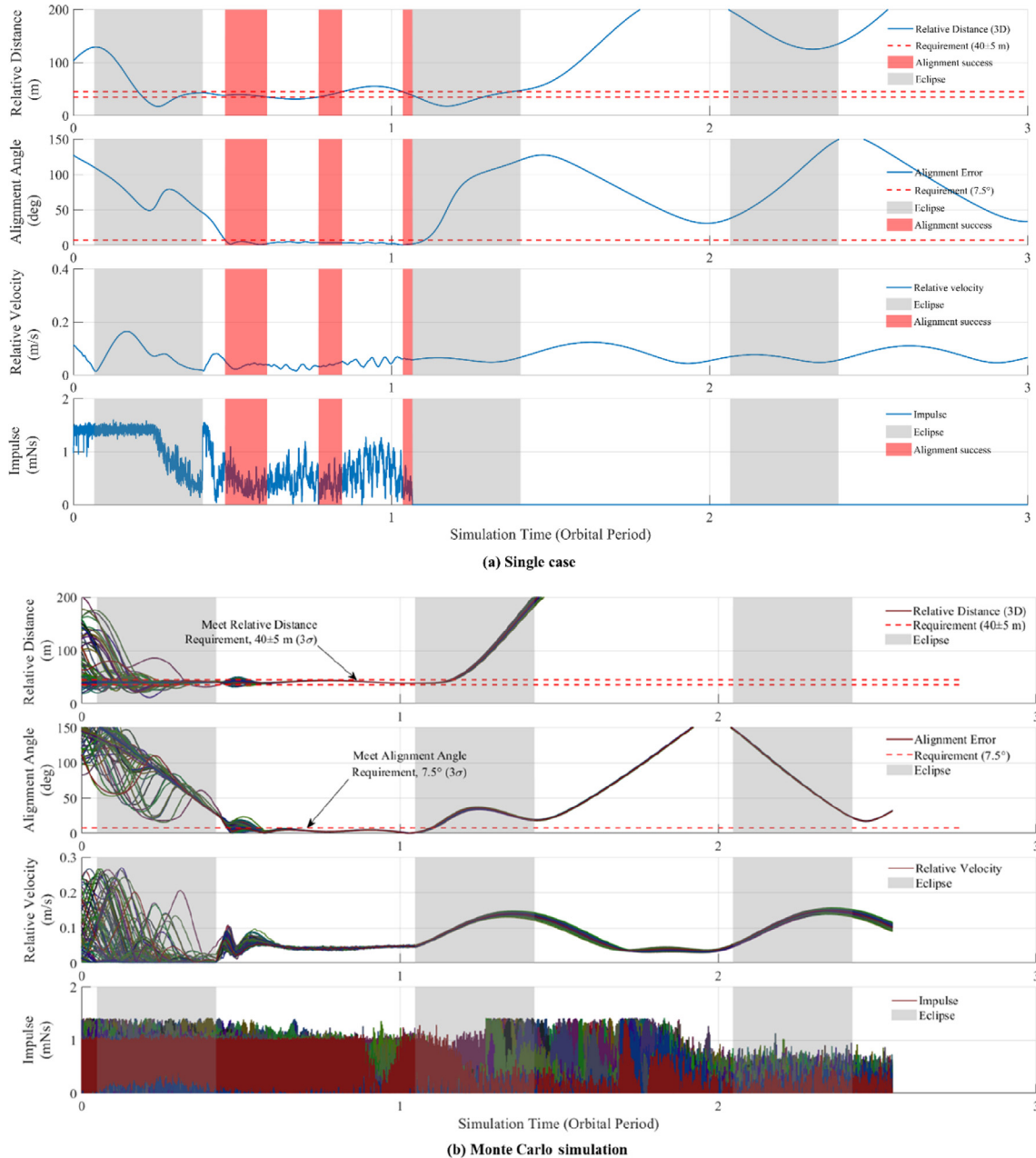


Fig. 15. Profiles of the relative distance, alignment angle, relative velocity, and impulse for the IAH; (a) single case, (b) 100 times the Monte Carlo simulation.

vibration testing, respectively. The values of f_0 measured on the deployable solar panels in the x-axis and y-axis ([Fig. 20](#) (a) and [Fig. 20](#) (b), respectively) are lower than f_0 on the structural frame ([Fig. 20](#) (c)). After the sine burst and random vibration testing, the values of f_0 measured on each axis decreased, and the variances in f_0 on the deployable solar panels are larger than f_0 on the structural frame, as presented in [Table 6](#). These phenomena are induced by the loosened nylon wire of the HRM on the solar panels and the wire's different tightening levels for each device. However, the minimum value exceeds 70 Hz, which is higher than the launch vehicle's requirement of 40 Hz

5.3.2. Thermal vacuum and cycling testing

The thermal space environment has extreme temperature changes and a vacuum, which causes thermal stress on the electronics and malfunctions. The testing setup is presented in [Fig. 21](#). According to the simulation results, the temperature range of the testing was set from -15 to 30 °C, while the vacuum level was lower than 3.0×10^{-4} torr. The thermocouples were attached to the exterior of each CubeSat. The temperature reference point (TRP) was set to the z-axis structural frame, where the temperature was most stable with thermal cycling. The chamber was controlled by the temperature of the TRP, and the

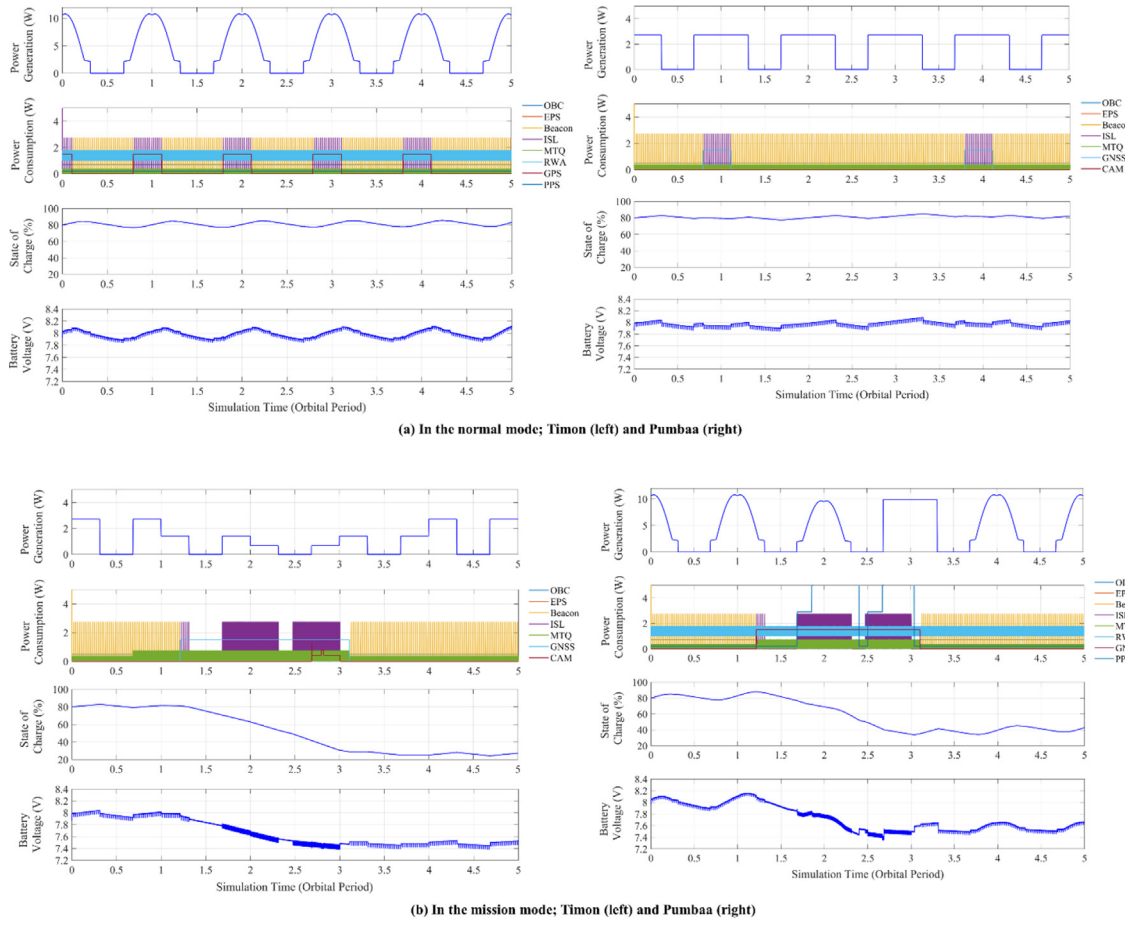


Fig. 16. Result of the energy balancing analysis with duty cycled operations and the battery's state of charge; (a) normal mode, (b) mission mode.

cycle consisted of two hot and cold cases. During the soaking time for the hottest and coldest cases, functional testing was performed to verify the functionalities of the components. In the coldest cases and transient periods below 0 °C, the heater on the propellant tank was tested to demonstrate the orbit maneuvers in the eclipse. Fig. 22 shows the temperature trend profile for each thermocouple.

For the soaking time's hottest case, the temperature of the OBC for both CubeSats increased to approximately 70 °C. Although the operation of the processor is slow, the tasks and scheduling on each OBC are processed well in real time. The PPS can be activated when the TRP temperature is below 0 °C. The heating duration for the propellant tank is affected by the external temperature; on the other hand, the nozzle is activated with short heating even in cold cases. The propellant tank was heated for more than 5 min before firing, and the heating duration for the nozzles required less than 1 min.

Before and after testing, the mass of each CubeSat was measured in order to estimate the outgassing of the components. The total mass loss (TML) values were 4 g for both CubeSats, which meets the TML requirements, and it is less than 1% of the total mass. From the results of the func-

tional testing in the hottest and coldest cases, this investigation verified that the electronics and devices on both CubeSats can endure the thermal space and vacuum environment while maintaining functionalities.

5.4. Systems specifications

As presented in Table 7, the system specifications of both CubeSats were evaluated by analysis and testing for the mission assurance to ensure they are sufficient to accomplish the mission. The specifications meet the assigned requirements. Timon can obtain images of the solar corona by utilizing a wide FOV camera. The 3-axis attitude control is performed by the air-coil-type MTQs on each axis. The attitude can be estimated through the EKF with the sun sensors, the IMU, and the MMT. To provide the GNSS measurement data to Pumbaa within 1 s, the ISL rate shall exceed 4.8 kbps, and Timon can perform ISL at a rate of 9.6 kbps, without any loss in the integrity of communication. The link margin is 3.8 dB at 15° for the minimum elevation while considering the circular polarization loss. With the body-mounted solar panels, Timon generates 2.0 W during the average orbit.

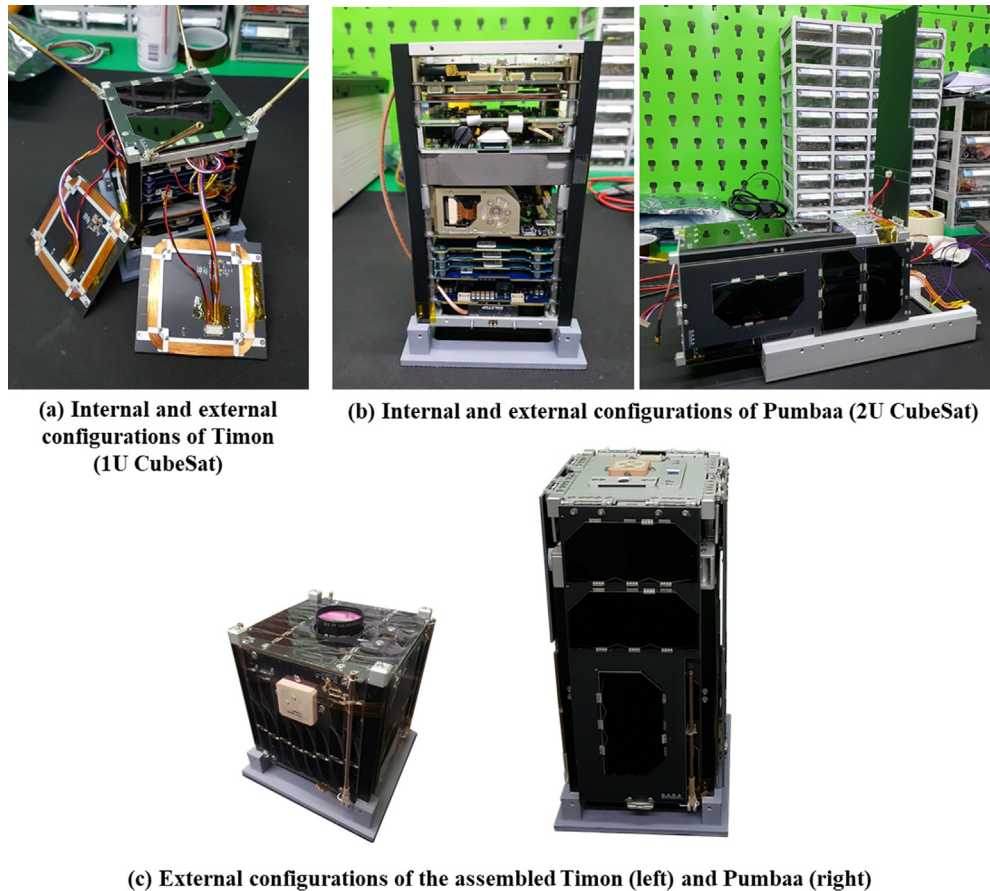


Fig. 17. Internal and external configurations; (a) Timon (1U CubeSat), (b) Pumbaa (2U CubeSat), (c) the integrated proto flight models of both CubeSats.

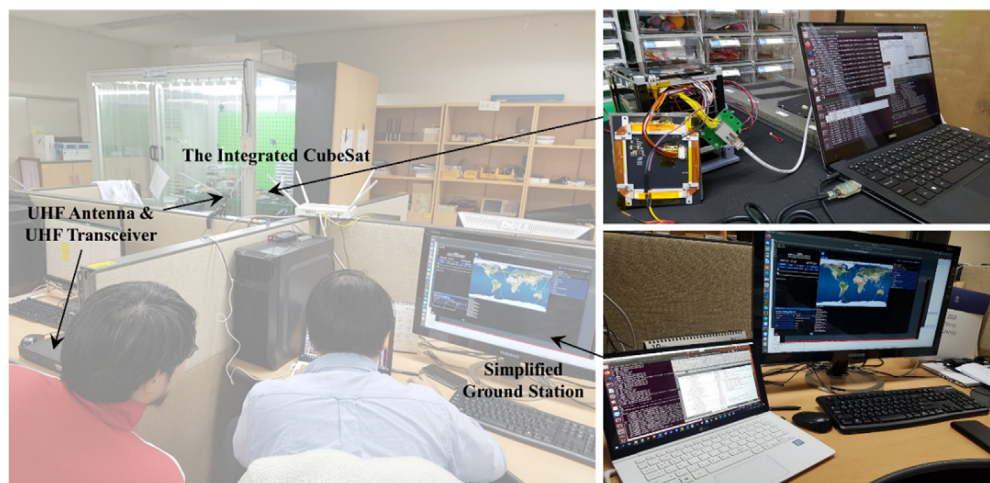


Fig. 18. Configuration of end-to-end testing with the RF communication.

In mission mode, Pumbaa and the Occulter block the light from the solar photosphere. When the stowed film is deployed, the Occulter enlarges to $0.75\text{ m} \times 0.75\text{ m}$. The 3-axis attitude control is performed with the combination of RWA and MTQs, which ensures precise pointing towards the sun within 5° in 3-sigma. The relative navigation based on the DGPS algorithm is precisely imple-

mented, and it then exhibits sub-meter accuracy levels in 3-sigma. The PPS enables precise orbit maneuvers such as the DRSK, rendezvous, and IAH. Given the complicated system limitations and hardware operations, Pumbaa consumes an electrical power of approximately 3 W in the normal mode. The deployable solar panels and body-mounted solar panels provide more than 5 W. The struc-

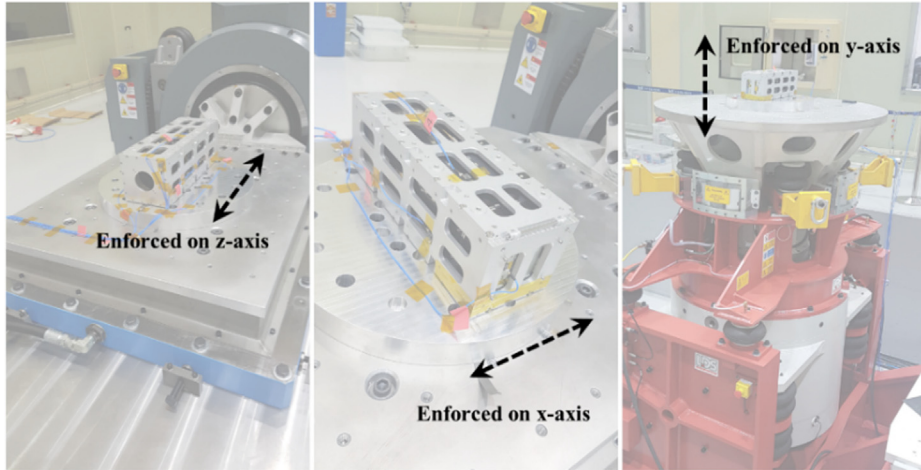


Fig. 19. Configuration of the vibration testing set-up.

Table 6
Variance of the first mode frequency before and after the vibration testing.

Coordinate		1st Mode Frequency (Hz)		Variance
Axis	Feature	Pre Survey	Post Survey	%
x	Deployable Solar Panel	96.03	76.98	19.83
y	Deployable Solar Panel	101.20	94.45	6.67
z	Structural Frame	160.50	153.60	4.30

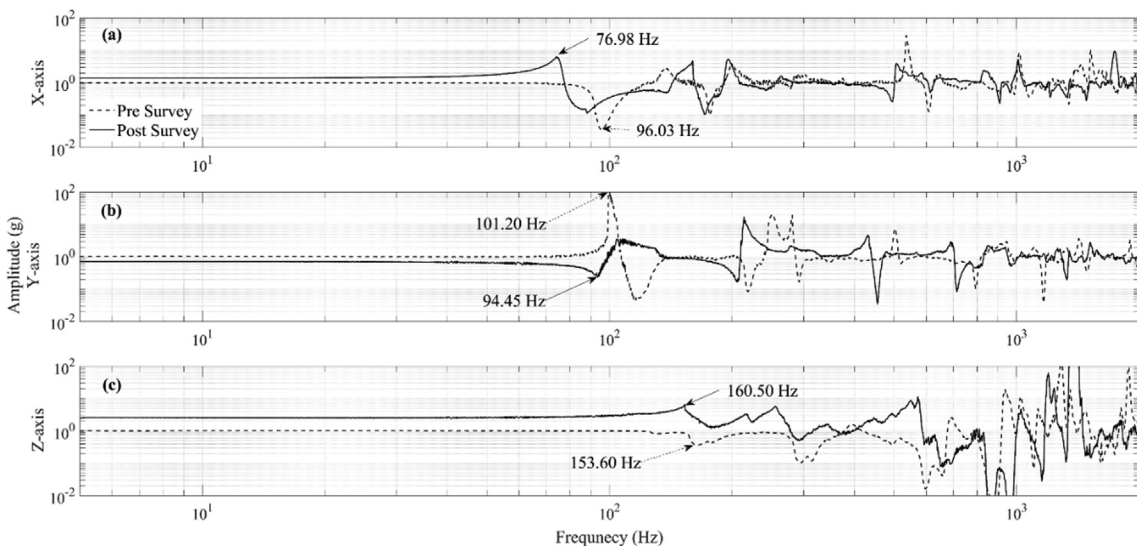


Fig. 20. Low level sine-sweep testing results: (a) the x-axis deployable solar panel, (b) the y-axis deployable solar panel, (c) and the z-axis structural frame.

tural stiffness is assured by the vibration testing, which is higher than 70 Hz in f_0 .

6. Conclusion

This paper introduced the solar science demonstration mission, which is based on CubeSat platforms, and outlined the development of the CubeSat systems for the CANYVAL-C mission. This mission aims to demonstrate solar science by implementing precise formation flying with

two CubeSats and obtaining several images of the solar corona. The CubeSat systems have limited resources and several constraints, such as the power capacity, the performance of the actuators and sensors, and the payload sizing. The concept of the operations was designed, and the mission requirements and constraints were then defined. Two CubeSats were developed with several verifications for mission assurance. Specifically, the systems were evaluated with numerical simulations, HILS, and testing, which included Monte Carlo simulations, end-to-end testing,

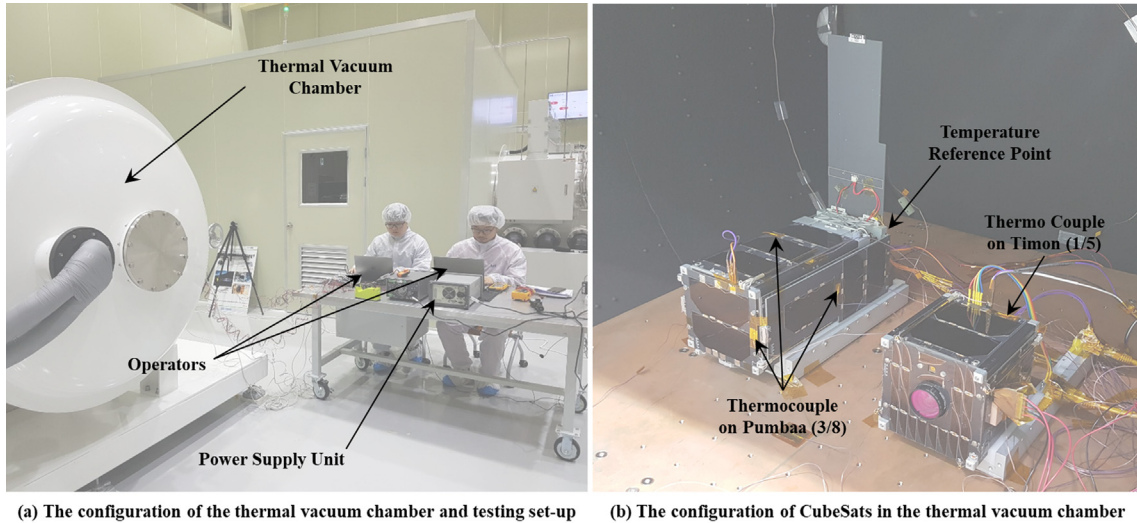


Fig. 21. Configuration of the thermal vacuum and cycling testing set-up.

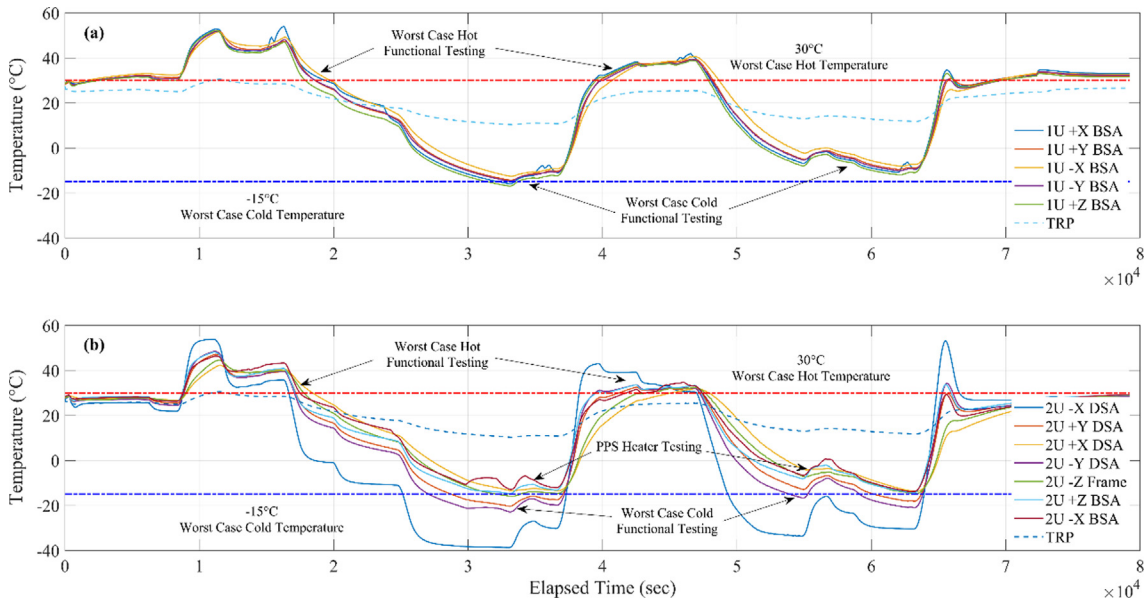


Fig. 22. Temperature trend of the thermocouples on each CubeSat;

and environmental testing. The specifications ensure the feasibility of the mission and the systems operation, which meet the requirements under several constraints. The significance of this study is that it provides the systems architecture for other formation flying missions that covers the constrained systems with limited resources. Consequently, this study is expected to contribute to advancement in technologies for next-generation space telescopes. Given the performance of the actuators and sensors, the mission requirements are less stringent than that of large-scale solar science missions. In the future, we plan to analyze the in-orbit data and improve the systems with the VT-based science mission by incorporating the CubeSat platforms.

Declaration of Competing Interest

The authors declare that they have no known competing financial interests or personal relationships that could have appeared to influence the work reported in this paper.

Acknowledgments

The authors would like to thank Mr. Philip Calhoun and Mr. Neerav Shah for supporting the NASA/Yonsei collaboration on the CANYVAL-C mission.

We would like to thank Editage (www.editage.co.kr) for English language editing.

Table 7
Specifications of the CubeSat systems.

(a) Timon (1U CubeSat)			
Contents	Requirements	Specifications	Remarks
Systems Lifetime	> 6 months	18 months	Total Ionizing Dose
Payload FOV	> 30.0°	33.4° × 43.5°	VFOV × HFOV
Orbit Determination (3σ)	< 50.0 m	10.5 m	Absolute, 3D RMS
Attitude Determination (3σ)	< 1.5° < 0.15°/s	< [0.92, 0.51, 0.61]° < [0.12, 0.11, 0.12]°/s	Each Axis, Daylight
Attitude Control (3σ)	< 5.0° < 0.5°/s	2.9° 0.2°/s	Sun-pointing Normally
Link Margin	> 3 dB	3.8 dB	At Elevation 15°
Date Rate	Uplink > 2.4 kbps Downlink > 4.8 kbps ISL > 4.8 kbps	4.8 kbps 9.6 kbps 9.6 kbps	Telecommand Telemetry, Mission Data Navigation Data
Power Generation	> 1.6 W	2.0 W	Orbit Average, Sun-pointing
Mass	< 1.33 kg	1.09 kg	–
Deployment Device	–	UHF Antenna	–
Separation Spring	–	2.04 N / 6.16 N	Initial / Final Force
(b) Pumbaa (2U CubeSat)			
Contents	Requirements	Specifications	Remarks
Systems Lifetime	> 6 months	18 months	Total Ionizing Dose
Payload Film Area	> 0.5 m × 0.5 m	0.75 m × 0.75 m	Fully Deployed
Dimension	< 0.5U	98 mm × 98 mm × 54 mm	Stowed
Orbit Determination (3σ)	< 50.0 m	10.5 m	Absolute, 3D RMS
Relative Orbit Control (3σ)	< 1.0 m	< [0.25, 0.44, 0.40] m	Relative, Each Axis
Attitude Determination (3σ)	< 3.0 m	< [2.97, 2.98, 2.86] m	Maximum, Each Axis
Attitude Control (3σ)	< 1.5° < 0.15°/s	< [1.20, 0.69, 0.61]° < [0.11, 0.11, 0.13]°/s	Each Axis, Daylight
Link Margin	< 3.0° < 0.5°/s	1.8° 0.2°/s	Sun-pointing Normally
Date Rate	Uplink > 2.4 kbps Downlink > 4.8 kbps ISL > 4.8 kbps	4.8 kbps 9.6 kbps 9.6 kbps	At Elevation 15° Telecommand Telemetry, Mission Data Navigation Data
Power Generation	> 4.0 W	5.1 W 8.3 W	Orbit Average, Nadir-pointing Orbit Average, Sun-pointing
Structural Stiffness	> 40 Hz	> 76.9 Hz	At Deployable Solar Panel
Mass	< 2.66 kg	2.56 kg	Wet Mass, 50 g of Propellant
Deployment Device	–	UHF Antenna, Deployable Solar Panels, Occulter	–
Separation Spring	–	2.04N / 6.16N	Initial / Final Force

Funding

This work was supported by the Space Basic Technology Development Program through the National Research Foundation (NRF) of Korea, funded by the Ministry of Science and the ICT of the Republic of Korea [grant number NRF-2017M1A3A3A06085349].

References

- Bandyopadhyay, S., Subramanian, G.P., Foust, R. et al., 2015. A review of impending small satellite formation flying missions. 53th AIAA Aerospace Sciences Meeting, Kissimmee, FL, USA. <https://doi.org/10.2514/6.2015-1623>.
- van Bolhuis, M.F., Lebbink, G.W., Overlack, A.E. et al., 2020. Environment Levels Auxiliary Payloads –ISILaunch27, ISL.ISILaunch27.EL, ISL – Innovative Space Logistics BV.
- Calhoun, P.C., Novo-Gradac, A.-M., Shah, N., 2018. Spacecraft alignment determination and control for dual spacecraft precision forma-
- tion flying. Acta Astronaut. 153, 349–356. <https://doi.org/10.1016/j.actaastro.2018.02.021>.
- Cho, D.-H., Choi, W.-S., Kim, M.-K., et al., 2019. High-resolution image and video CubeSat (HiREV): Development of space technology test platform using a low-cost CubeSat platform. Int. J. Aerosp. Eng. <https://doi.org/10.1155/2019/8916416>.
- Denis, G., Alary, D., Pasco, X., et al., 2020. From new space to big space: How commercial space dream is becoming a reality. Acta Astronaut. 166, 431–443. <https://doi.org/10.1016/j.actaastro.2019.08.031>.
- Dennis, B.R., Skinner, G.K., Li, M.J., et al., 2013. Very high-resolution solar x-ray imaging using diffractive optics. Solar Phys. 279, 573–588. <https://doi.org/10.1007/s11207-012-0016-7>.
- Fu, B., Sperber, E., Eke, F., 2016. Solar sail technology – A state of the art review. Prog. Aerosp. Sci. 86, 1–19. <https://doi.org/10.1016/j.paerosci.2016.07.001>.
- Gao, L., Liu, S., 2002. Dynamic lithium-ion battery model for system simulation. IEEE Trans. Comp. Pack. Tech. 25 (3), 495–505. <https://doi.org/10.1109/TCAPT.2002.803653>.
- GomSpace, NanoCam CIU, <https://gomspace.com/home.aspx>, 2020 (accessed 16 April 2020).

- GomSpace, NanoProp CGP3, <https://gomspace.com/home.aspx>, 2020 (accessed 15 April 2020).
- Kim, G.-N., Park, S.-Y., Kang, D.-E. et al., 2019. Development of CubeSats for CANYVAL-C mission in formation flying, 11th Asia Pacific International Symposium on Aerospace Technology, Gold Coast, Australia, p. 802.
- Landini, F., Vives, S., Venet, M., et al., 2011. External occulter laboratory demonstrator for the forthcoming formation flying coronagraphs. *Appl. Opt.* 50 (36), 6632–6644. <https://doi.org/10.1364/AO.50.006632>.
- Lee, E., Son, J., Park, S.-Y., 2021. Relative navigation technique with constrained GNSS data for formation-flying CubeSat mission. *CANYVAL-C. Nav.*, 1–17 <https://doi.org/10.1002/navi.439>.
- Lee, Y., Park, S.-Y., Park, J.-P., et al., 2019. Numerical analysis of relative orbit control strategy for CANYVAL-X mission. *J. Astron. Space Sci.* 36 (4), 235–248. <https://doi.org/10.5140/JASS.2019.36.4.235>.
- Leung, S., Montenbruck, O., 2005. Real-time navigation of formation-flying spacecraft using global-positioning-system measurement. *J. Guid. Contr. Dynam.* 28 (2), 226–235. <https://doi.org/10.2514/1.7474>.
- Mason, J.P., Woods, T.N., Chamberlin, P.C., et al., 2020. MinXSS-2 cubesat mission overview: Improvements from the successful MinXSS-1 mission. *Adv. Space Res.* 66 (1), 3–9. <https://doi.org/10.1016/j.asr.2019.02.011>.
- Millan, R.M., von Steiger, R., Ariel, M., et al., 2019. Small satellites for space science: A COSPAR science roadmap. *Adv. Space Res.* 64 (8), 1466–1517. <https://doi.org/10.1016/j.asr.2019.07.035>.
- Misra, P., Enge, P., 2011. Global Positioning System: Signals, Measurements, and Performance, second ed., Ganga-Jamuna Press.
- NASA/GSFC, Core Flight System, <https://cfs.gsfc.nasa.gov/>, 2020 (accessed 16 April 2020).
- Newman, J.Z., 2015. Drift recovery and station keeping for the CanX-4 & CanX-5 nanosatellite formation flying mission (Master's Thesis). University of Toronto. <https://search.proquest.com/docview/1728159405> (accessed 16 April 2020).
- Park, S.-Y., Calhoun, P.C., Shah, N. et al., 2014. Orbit design and control of technology validation mission for refractive space telescope in formation flying, AIAA Guidance, Navigation, and Control Conference, SciTech 2014, National Harbor, Maryland, USA. <https://doi.org/10.2514/6.2014-0451>.
- Park, J.-P., Park, S.-Y., Song, Y.B., et al., 2016. CubeSat development for CANYVAL-X mission. In: 14th International Conference on Space Operations, Deajeon, Korea. <https://doi.org/10.2514/6.2016-2493>.
- Romoli, M., Antonucci, E., Fineschi, S. et al., 2003. The ultraviolet and visible-light coronagraph of the HERSCHEL experiment, Proceedings of the 10th International Solar Wind Conference, 679(1), p. 846. <https://doi.org/10.1063/1.1618723>.
- Roscoe, C.W.T., Westphal, J.J., Mosleh, E., 2018. Overview and GNC design of the CubeSat proximity operations demonstration (CPOD). *Acta Astronaut.* 153, 410–421. <https://doi.org/10.1016/j.actaastro.2018.03.033>.
- Roth, N.H., 2010. Navigation and control design for the CanX-4/5 satellite formation flying mission (Master's Thesis). University of Toronto. https://tspace.library.utoronto.ca/bitstream/1807/25908/3/Roth_Niels_H_201011_MASc_thesis.pdf (accessed 16 April 2020).
- Shah, N., Calhoun, P.C., Dennis, B.R. et al., 2013. The virtual telescope demonstration mission, 5th International Conference on Spacecraft Formation Flying Missions and Technologies, Munich, Germany.
- Skinner, G.K., Arzoumanian, Z., Cash, W.C., et al., 2008. The milli-arc-second structure imager (MASSIM): A new concept for a high angular resolution x-ray telescope. *Proc. SPIE* 7011. <https://doi.org/10.1117/12.789568>.
- SKC Kolon PI, 2020. Black Polyimide Film, <http://www.skckolonpi.com/main/index.jsp.html> (accessed 15 April 2020).
- Seager, S., Turnbull, M., Sparks, W., et al., 2015. The Exo-S probe class Starshade mission. *Proc. SPIE* 9605. <https://doi.org/10.1117/12.2190378>.
- Song, S., 2016. System design and analysis of solar sail deployment for cube satellite CNUSAIL-1 (Master's Thesis). Chungnam National University. http://dcollection.cnu.ac.kr/public_resource/pdf/00000066949_20200416110407.pdf (accessed 16 April 2020).
- SPENVIS Website, 2020. <https://www.spenvis.oma.be> (accessed 16 April 2020).
- Underwood, C., Pellegrino, S., Lappas, V.J., et al., 2015. Using CubeSat/micro-satellite technology to demonstrate the autonomous assembly of a reconfigurable space telescope (AAReST). *Acta Astronaut.* 114, 112–122. <https://doi.org/10.1016/j.actaastro.2015.04.008>.
- Vives, S., Lamy, P., Koutchmy, S. et al., 2009. ASPIICS, A giant externally occulted coronograph for the PROBA-3 formation flying mission, *Adv. Space Res.* 43 (6) 1007–1012. <https://doi.org/10.1016/j.asr.2008.10.026>.
- Villalva, M.G., Gazoli, J.R., Filho, E.R., 2009. Comprehensive approach to modelling and simulation of photovoltaic arrays. *IEEE Trans. Power Electronics.* 24 (5), 1198–1208. <https://doi.org/10.1109/TPEL.2009.2013862>.
- Welle, R.P., Hinkley, D., 2014. The aerospace nano/picosatellite program. https://www.nasa.gov/sites/default/files/files/D_Hinkley-Aerospace_PICOSAT_Capability_Status_2014.pdf (accessed 15 April 2020).